

Topology optimization of flexible micro-fluidic devices

Sebastian Kreissl · Georg Pingen · Anton Evgrafov · Kurt Maute

Received: 10 September 2009 / Revised: 30 March 2010 / Accepted: 21 May 2010 / Published online: 12 June 2010
© Springer-Verlag 2010

Abstract A multi-objective topology optimization formulation for the design of dynamically tunable fluidic devices is presented. The flow is manipulated via external and internal mechanical actuation, leading to elastic deformations of flow channels. The design objectives characterize the performance in the undeformed and deformed configurations. The layout of fluid channels is determined by material topology optimization. In addition, the thickness distribution, the distribution of active material for internal actuation, and the support conditions are optimized. The coupled fluid-structure response is predicted by a non-linear finite element model and a hydrodynamic lattice Boltzmann method. Focusing on applications with low flow velocities and pressures, structural deformations due to fluid-forces are neglected. A mapping scheme is presented that

couple the material distributions in the structural and fluid mesh. The governing and the adjoint equations of the resulting fluid-structure interaction problem are derived. The proposed method is illustrated with the design of tunable manifolds.

Keywords Fluid-structure interaction · Hydrodynamic lattice Boltzmann method · Non-linear elasticity · Adjoint sensitivity analysis

1 Introduction

This study focuses on topology optimization of dynamically tunable fluidic devices. The basic idea of the proposed design concept is to embed flow channels into a flexible structure that deforms in response to externally or internally applied mechanical loads. The primary goal is to optimize the layout of the elastically deforming fluid channels with respect to multiple objectives, characterizing the device in the deformed and undeformed configurations. To further enhance the device performance, the stiffness distribution, the layout of the actuation system, as well as the support conditions of the device are also optimized.

Topology optimization is a well established method for designing structural systems (Bendsøe and Sigmund 2003; Ramm et al. 1998a, b). For an overview of structural topology optimization the reader is referred to the manuscript by Bendsøe and Sigmund (2003). Topology optimization of flow problems was pioneered by Borrvall and Petersson (2003). In their initial study a Stokes flow model was employed. This approach has further been generalized in a number of ways (Andreasen et al. 2009; Gersborg-Hansen et al. 2005; Evgrafov 2006; Aage et al. 2008; Klimetzek

Preliminary results of the work presented in this paper have been published in the proceedings of WCSMO-8, Lisbon, Portugal, 2009.

S. Kreissl · K. Maute (✉)
Center for Aerospace Structures,
University of Colorado at Boulder,
Boulder, CO, USA
e-mail: maute@colorado.edu

S. Kreissl
e-mail: kreissl@colorado.edu

G. Pingen
Department of Mechanical and Aerospace Engineering,
University of Colorado at Colorado Springs,
Colorado Springs, CO, USA
e-mail: gpingen@eas.uccs.edu

A. Evgrafov
Department of Mathematics,
Technical University of Denmark,
Lyngby, Denmark
e-mail: a.evgrafov@mat.dtu.dk

et al. 2006; Moos et al. 2004; Othmer et al. 2006; Othmer 2008). As an alternative to the Navier–Stokes flow model, Pingen et al. used the lattice Boltzmann method (LBM) to solve fluid topology optimization problems (Pingen 2008; Pingen et al. 2007a, b, 2009a, b).

Topology optimization of fluid–structure systems has hardly been studied so far. Guest and Prévost (2006) maximized the stiffness while simultaneously maximizing the fluid permeability of periodic materials. Although a fluid–structure interaction system was considered, no interaction between fluid and solid was taken into account in this study. Maute and Allen (2004) and Maute and Reich (2006) optimized the internal layout of structures accounting for coupling between flow and structural deformation. However, this approach only allows for changes of the shape but not the topology of the fluid–solid interface. Yoon (2009) recently introduced a monolithic formulation for topology optimization of fluid–structure interaction (FSI) problems. While this approach considers a fully coupled FSI system, it is limited to small structural deformations.

In this study we present a topology optimization method for FSI problems undergoing large elastic deformations. We focus on micro–fluidic devices with flow channels sandwiched between two elastically deforming structural layers. Owing to the low flow velocity in micro channels, the fluid pressure exerted on the structure is typically negligible in comparison to the stiffness of the structure. However, large deformations are needed to noticeably alter the flow due to mechanical actuation. Therefore, we consider only the effect of finite structural deformations on the flow field and disregard the influence of the fluid forces on the structural deformations, leading to a one–way structure–fluid coupling. We will show quantitatively with a numerical example that the fluid forces only have a negligible effect on the structural solution for the class of micro–fluidic devices considered in this study.

Following a standard material topology optimization approach, the geometry of the flow channels is described by a material distribution function. Additional optimization parameters are used to control the thickness distribution, the distribution of active material for internal actuation, and the support conditions of the device. The structural response is described by a non–linear finite element model using a total Lagrangian formulation. The flow is predicted by a hydrodynamic LBM operating on a fixed grid. The material distributions in the deforming structural mesh and fixed fluid mesh are coupled by a geometric mapping approach, as shown in Fig. 1. Contrary to a monolithic approach (Yoon 2009), the separate treatment of the fluid and structural domain allows to employ existing analysis modules: in the current study, an LBM fluid solver and a geometrically non–linear FEM structural solver. We consider optimization problems involving the fluid and structural

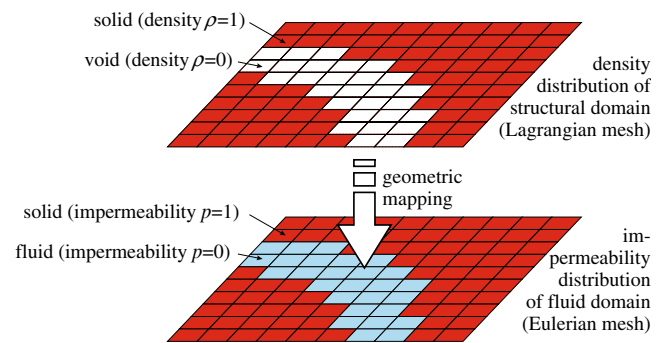


Fig. 1 Separate meshes for structural and fluid domain

behavior in the undeformed and deformed configuration at steady–state. These problems are cast into a multi–objective formulation and solved by a gradient based optimization algorithm computing the design sensitivities by an adjoint method.

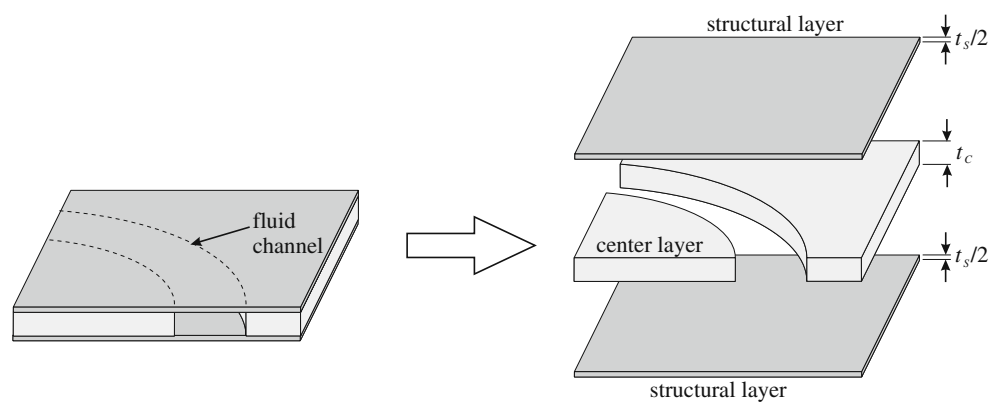
In this paper we present an optimization method for a one–way coupled FSI problem using a material distribution approach to describe the geometry of the fluid and structural domains. We present details of the geometric mapping method that couples the material distribution in the fluid and structural meshes. We derive the adjoint of this system and discuss its computational complexity. The utility of the proposed approach is illustrated with three numerical examples. The remainder of the paper is organized as follows. In Sections 2 and 3 we describe the design and structural model. Section 4 outlines the basics of the LBM. This is followed by a description of the geometrical mapping from the structural domain into the fluid domain in Section 5. Section 6 describes the overall computational optimization procedure along with the sensitivity analysis. Finally, we demonstrate the key features of our approach with three 2–D numerical examples in Section 7. The results are summarized in Section 8.

2 Design models

Focusing on micro–fluidic devices, which are typically fabricated by micro–surface, bulk machining or layer deposition techniques, we consider structures that consist of multiple layers. In this paper, we focus on a three–layer design (see Fig. 2): the center layer houses the embedded fluid channels and is sandwiched between two structural layers, which provide structural support for the center layer and prevent evaporation and leakage.

To manipulate the design we consider four sets of optimization variables: (1) The layout of the flow channels in the center layer is described by a material distribution function. The material properties are defined via smooth interpolation functions depending on the optimization

Fig. 2 Structural system



variables $s_m^i \in [0, 1]$. (2) The thickness distribution of the structural layers is defined by the optimization variables $s_t^i \in [0, 1]$. (3) The locations where the structural layers are attached to a ground structure are described by the distribution of the support stiffness which is defined by the optimization variables $s_s^i \in [0, 1]$. (4) The layout of active material embedded into the structural layers is described via the distribution of eigenstrains. In this study only isotropic eigenstrains ϵ_e are considered which are defined by the independent optimization variables $s_e^i \in [-1, 1]$. The four sets of optimization variables are combined into the design vector $\mathbf{s} = [s_m \ s_t \ s_s \ s_e]$.

By controlling the thickness of the structural layers via s_t^i we can tailor the stiffness independently from the layout of the layer that houses the fluid channels. This allows, for example, to stiffen areas beneath a flow channel or to soften areas beneath a solid center layer. To illustrate this issue, Fig. 3 shows the structural layout of a simple channel subject to a compressive load. The structure is fixed along the left and right edges. As the stiffness in the center layer along the channel is negligible, the pressure drop across the channel in the deformed configuration depends only on the stiffness of the structural layers, which can

be controlled conveniently by the thickness. For practical applications, these thickness variations could be fabricated via layer deposition techniques (Kim et al. 2009) or 3D printing methods (Dimitrov et al. 2006).

The basic concept of varying the support stiffness is illustrated in Fig. 4. Imposing a large value for the support stiffness at a point, the structural displacements vanish and the point can be considered fixed (Babuška 1973). Manipulating the support stiffness has a similar but more pronounced effect compared to varying the thickness of the structural layers. While both alter the stiffness of the structure, their effect on the overall displacement field differs, as illustrated in Fig. 5. For example, increasing the value of the thickness variable s_t primarily reduces the deformation locally, within the stiffened region ($b^d \approx b^u$ in Fig. 5b). Increasing the support stiffness has a global effect and shields the left part of the structure from deforming ($a^d \approx a^u$ and $b^d \approx b^u$ in Fig. 5c). In practice this could be realized, for example via adhesive bonding techniques (Niklaus et al. 2006). Depending on the fabrication approach used to vary the thickness of the structural layers, the surface topography of the substrate may also have to be altered to allow bonding of the structural layer to the substrate.

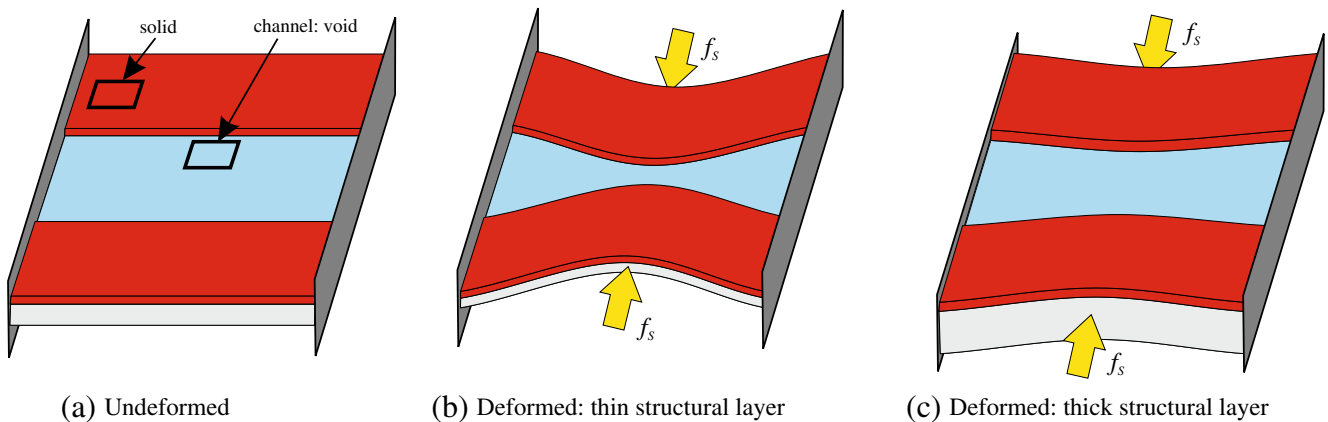


Fig. 3 Influence of thickness of the structural layers on the stiffness (for visualization only the bottom structural layer is shown)

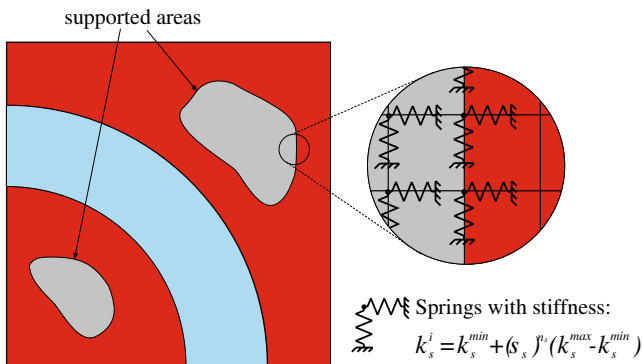


Fig. 4 Support layout (cp. Buhl 2002)

In particular in micro-fluidic applications, forces are conveniently generated by active materials embedded into the structural layers, such as piezo-ceramic or electro-active polymers (Bar-Cohen 2004; Zhang et al. 2005). Optimizing the layout of active materials in concert with the thickness of the structural layers and the distribution of the support stiffness allows fine-tuning of the structural deformations. The effect of active materials on the overall device is modeled by introducing eigenstrains into the constitutive equations of the structural layers.

3 Structural model

To alter low-speed flows, large changes of the channel geometry and thus large deformations of the structure are

required. Therefore, the structural response is described by a geometrically non-linear finite element (FE) model. For the sake of simplicity, we assume a linear stress–strain relationship in this study. However, for a more realistic modeling of the structural response, especially when dealing with large strains, a non-linear stress–strain model would be more appropriate. We further assume that the thickness is much smaller than the in-plane dimensions of the structure and the structural response can be approximated by a plane-stress model.

The four sets of optimization variables defined previously are introduced into the structural FE model via interpolation functions, the corresponding interpolation parameters are summarized in Table 1. Following the standard notation in topology optimization, the density ρ^i and Young’s modulus E_C^i of the center layer of the i -th element are defined by:

$$\rho^i = s_m^i \rho^{solid} \tag{1}$$

$$E_C^i = s_m^i E_C^{max} \tag{2}$$

The total Young’s modulus of the layered structure is computed by weighting the Young’s moduli of the layers with their thickness fractions:

$$E = E_C \left(\frac{t_C}{t} \right) + E_S \left(\frac{t_S}{t} \right) \quad \text{with } t = t_C + t_S \tag{3}$$

where t_C , t_S and E_S define thicknesses of the center layer, the structural layers and Young’s modulus of the structural

Fig. 5 Effect of thickness variation vs. support variation on structural displacement field

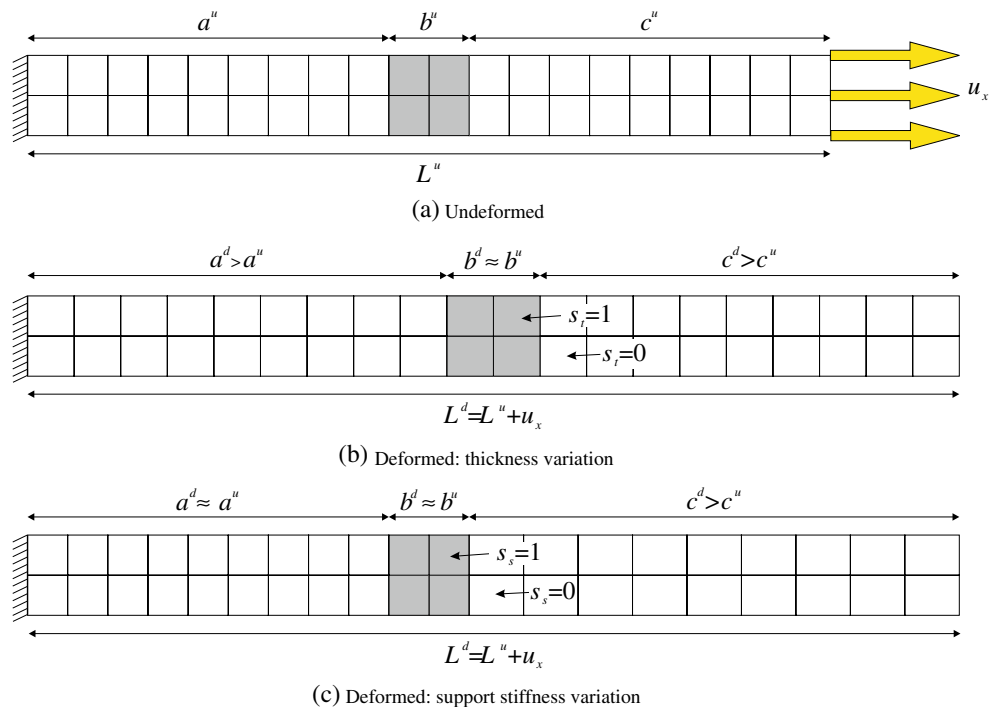


Table 1 Parameters for structural interpolation functions

Interpolated quantity	Parameter	Meaning
Density	ρ^i	Elemental density
	ρ^{solid}	Density of completely solid bulk material
Young’s modulus	E_C^i	Elemental Young’s modulus of center layer
	E_C^{max}	Maximum Young’s modulus of center layer
Thickness	t_S^i	Elemental thickness of structural layers
	t_S^{min}	Minimum elemental thickness of structural layers
	t_S^{max}	Maximum elemental thickness of structural layers
Support stiffness	k_s^{min}	Minimum support stiffness
	k_s^{max}	Maximum support stiffness
Eigenstrain	ϵ_{eig}^{min}	Minimum eigenstrain
	ϵ_{eig}^{max}	Maximum eigenstrain

layers, respectively. The thickness of the structural layers for the i -th element is given by:

$$t_S^i = t_S^{min} + s_e^i (t_S^{max} - t_S^{min}) \tag{4}$$

where t_S^{min} and t_S^{max} are the minimum and maximum elemental thicknesses of the structural layer.

Following the work of Buhl (2002), a spring model with variable stiffness is used to smoothly vary the support conditions from ‘moving freely’ to ‘fully clamped’. The spring stiffness k_s^i associated with the nodes of the i -th element are defined as:

$$k_s^i = k_s^{min} + s_e^i (k_s^{max} - k_s^{min}) \tag{5}$$

where k_s^{min} and k_s^{max} are the minimum and maximum support stiffnesses, respectively. A minimum support stiffness larger than zero is chosen to prevent rigid body motions and numerical ill-conditioning. For a value of $s_e^i = 1$ the support stiffness leads to negligible nodal displacements. Note that this approach acts only as a vehicle for determining the optimal locations for the supports and therefore the linear springs pose no inconsistency with the geometrically non-linear structural description.

The eigenstrains are interpolated linearly as follows:

$$\epsilon_e^i = s_e^i \epsilon_{eig}^{max} \tag{6}$$

The elemental eigenstrain ϵ_e^i enters the non-linear plane-stress formulation via the constitutive model assuming a

linear elastic material behavior and an additive decomposition of the elastic and inelastic strains. The total nominal stress is defined e.g. in Belytschko et al. (2005):

$$\mathbf{P} = \mathbf{S} \cdot \mathbf{F}^T \quad \text{with} \quad \mathbf{S} = \mathbf{C} : (\mathbf{E} - \mathbf{E}^{eig}) \tag{7}$$

where \mathbf{F} is the deformation gradient and \mathbf{S} denotes the second Piola–Kirchhoff stress tensor. The stress depends on the material tensor \mathbf{C} , the total Green-Lagrange strain \mathbf{E} and the inelastic isotropic eigenstrains \mathbf{E}^{eig} . The latter are defined as an explicit function of the optimization variables s_e via the interpolation (6):

$$\mathbf{E}^{eig} = \begin{bmatrix} \epsilon_e & 0 \\ 0 & \epsilon_e \end{bmatrix} \tag{8}$$

From the total nominal stress we obtain the internal force \mathbf{f}_S^{int} , for example see Belytschko et al. (2005):

$$\mathbf{f}_S^{int} = \int_{A_0} \mathbf{B}_0^T \mathbf{P} t \, dA_0, \tag{9}$$

where A_0 is the area and \mathbf{B}_0 is the differential operator in the undeformed configuration.

The support stiffness leads to an additional force \mathbf{f}_S^k :

$$\mathbf{f}_S^k = \mathbf{K}_s \mathbf{u}, \quad \text{with} \quad \mathbf{K}_s = k_s^i \mathbf{I} \tag{10}$$

where \mathbf{K}_s is the stiffness matrix associated with the support layout, \mathbf{u} are the displacements, and \mathbf{I} is an identity matrix.

Given the internal forces, $\mathbf{f}_S^{int} + \mathbf{f}_S^k$ and the external loads, \mathbf{f}_S^{ext} , the structural residual \mathbf{R}_S governing the static response is written as:

$$\mathbf{R}_S(\mathbf{u}, \mathbf{s}) = \mathbf{f}_S^{int}(\mathbf{u}, \mathbf{s}) + \mathbf{f}_S^k(\mathbf{u}, \mathbf{s}) - \mathbf{f}_S^{ext} = \mathbf{0}, \tag{11}$$

The above system of non-linear equations, (11), is solved by Newton’s method.

4 Flow model

In this study we approximate the flow in the channels by a two-dimensional model assuming a uniform flow across the channel thickness. This approach neglects friction effects along the bottom of the channels and leads to approximations in predicting drag and pressure drop values. To capture the influence of no-slip conditions at the top and bottom layers, Borrvall and Petersson (2003) introduced an explicit approximation of the flow in thickness direction. As previous work by the authors on fluid topology optimization (Pingen et al. 2007a, b) has shown, the 2-D flow model leads to optimization results equivalent to the ones presented

in Borrvall and Petersson (2003). Therefore, the 2-D model is considered sufficient for the present study. However, it should be noted that in general the friction at the bottom/top of the channel may influence the flow solution.

Motivated by previous theoretical and numerical studies (Pingen 2008; Pingen et al. 2007a; Evgrafov et al. 2008), we choose a hydrodynamic LBM to predict the channel flow. The hydrodynamic LBM approximates the Navier–Stokes equations for low Mach number flows (Chen and Doolen 1998; Succi 2001; Yu et al. 2003). It can be derived from the Boltzmann transport equation which is typically discretized by an explicit finite difference scheme in space and time, constituting a two step time-marching process:

Collision: $\tilde{f}_\alpha(\mathbf{x}_i, t) = f_\alpha(\mathbf{x}_i, t) - \frac{1}{\tau} [f_\alpha(\mathbf{x}_i, t) - f_\alpha^{eq}(\mathbf{x}_i, t)],$ (12)

Propagation: $f_\alpha(\mathbf{x}_i + \delta t \mathbf{e}_\alpha, t + \delta t) = \tilde{f}_\alpha(\mathbf{x}_i, t),$ (13)

where \mathbf{e}_α is the velocity vector, f_α is the distribution function associated with the corresponding velocity \mathbf{e}_α , \mathbf{x}_i represents the location in physical space, $\mathbf{e}_\alpha \delta t$ is the lattice spacing, δt is the time step, $\tau = \lambda/\delta t$ is the dimensionless relaxation time, and $f^{eq} = f^{eq}(\bar{\rho}, \mathbf{w})$ is a Taylor series approximation of the Maxwell–Boltzmann equilibrium distribution. The macroscopic parameters (fluid density $\bar{\rho}$, velocity \mathbf{w} , pressure, and viscosity) can be evaluated via statistical moments of the distribution function f . Approximating the channel flows by a two-dimensional model, we use the D2Q9 lattice scheme (see e.g. Yu et al. 2003) in the current study.

To solve the topology optimization problem by gradient-based schemes, the LBM is augmented with the porosity model introduced by Spaid and Phelan (1997), providing a continuous transition from fluid to solid and vice versa. The macroscopic velocity \mathbf{w} is rescaled during the collision step (12), leading to:

$$\tilde{\mathbf{w}}^j(t, \mathbf{x}) = \left(1 - p^j(\mathbf{x})^\kappa\right) \mathbf{w}^j(t, \mathbf{x}), \tag{14}$$

where $p^j(\mathbf{x})$ is the impermeability that is related to the porosity in the domain. The vector $\tilde{\mathbf{w}}(t, \mathbf{x})$ defines the scaled velocity through porous media, which is substituted into the equilibrium distribution function $f^{eq}(\bar{\rho}, \tilde{\mathbf{w}})$ in place of \mathbf{w} . Note, that the interpolation of the impermeability p^j is defined analogously to the interpolation of the structural density ρ^i : $p^j, \rho^i = 1$ corresponds to *solid* and $p^j, \rho^i = 0$ corresponds to *fluid*, respectively *void* for the structure. The impermeability distribution $p(\mathbf{x})$ in the flow model is a function of the material distribution $\rho(\mathbf{x})$ in the structural domain and the structural displacements, \mathbf{u} .

Numerical studies show that this porosity approach converges to a 0–1 distribution; best results were obtained for an exponent $\kappa \approx 3$ (Pingen et al. 2009a). Due to the element wise constant impermeability values, this approach results in stair-step boundaries. However, Pingen et al. (2009a) have shown in numerical studies that this porosity approach captures the flow characteristics—e.g. pressure drop, drag, etc.—sufficiently well, especially for the low Reynolds numbers considered in the current study.

In the current study we focus on steady-state flows which are described by the solution of the following fixed-point problem:

$$\mathbf{R}_F(\mathbf{f}, \mathbf{s}) = \mathbf{M}(\mathbf{f}, \mathbf{s}) - \mathbf{f} = \mathbf{0}, \tag{15}$$

where \mathbf{R}_F denotes the fluid residual vector and \mathbf{f} describes the fluid state. The operator \mathbf{M} performs one collision (12) and one propagation (13), which corresponds to advancing the flow solution one time step by an explicit time integration scheme. We solve the fixed-point problem (15) by an explicit time-marching scheme advancing the flow until convergence toward steady-state. While this approach is memory efficient, it requires a relatively large number of time-steps to reach steady-state convergence.

5 Coupling structural and fluid domains

To couple the structural domain with the fluid domain a simple geometric mapping that transforms structural densities into fluid impermeabilities is employed. The basic concept is illustrated in Figs. 1 and 6. The structural densities, ρ^i , are defined on a deforming mesh using a Lagrangian formulation, whereas the impermeabilities, p^j , of the fluid are defined on a fixed mesh in an Eulerian formulation. The mapping is given by:

$$p^j(\rho^i, \mathbf{u}^i) = \frac{1}{A_F^j} \sum_{i=1}^{n_j} \left(\frac{\rho^i}{\rho^{solid}} A_{int}^{ij}(\mathbf{u}^i) \right). \tag{16}$$

The index i describes the structural elements that intersect with the j -th fluid element, A_{int}^{ij} is the intersection area between the i -th structural and the j -th fluid element, and A_F^j defines the area of the fluid element.

The impermeability of a fluid element p^j , (16), depends on (I) the densities of the underlying structural mesh, ρ^i , and (II) the deformation \mathbf{u}^i of the Lagrangian mesh, as the mesh-geometry of the structural mesh affects the intersection areas A_{int}^{ij} . Note, that ρ^i defines the elemental structural density, cp. (1), in the undeformed configuration and is therefore, unlike the impermeability p^j , independent of the displacements \mathbf{u}^i .

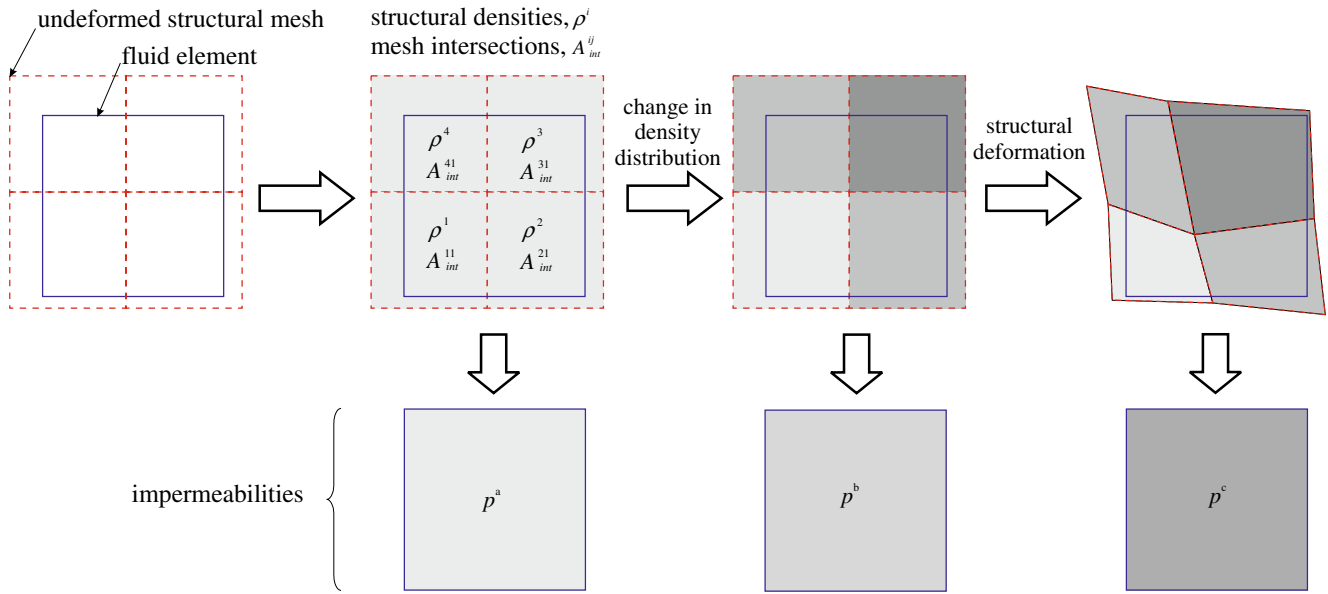


Fig. 6 Geometric mapping

6 Topology optimization of fluid-structure system

In this study we consider optimization problems of the following form:

$$\min_{\mathbf{s}} z = z(\mathbf{s}, \mathbf{u}^u(\mathbf{s}), \mathbf{f}^u(\mathbf{s}), \mathbf{u}^d(\mathbf{s}), \mathbf{f}^d(\mathbf{s})),$$

$$\text{s.t.} \begin{cases} \mathbf{s}, & \text{satisfy the design constraints,} \\ \mathbf{u}^{u,d}, & \text{solve (11) for given } \mathbf{s}, \\ \mathbf{f}^{u,d}, & \text{solve (15) for given } \mathbf{s}, \\ \mathbf{h}(\mathbf{s}, \mathbf{f}^{u,d}) = \mathbf{0}, & \text{the equality constraints,} \\ \mathbf{g}(\mathbf{s}, \mathbf{f}^{u,d}) \leq \mathbf{0}, & \text{the inequality constraints,} \end{cases} \quad (17)$$

where z is a scalar performance functional constructed from a multi-objective formulation of the design problem; \mathbf{s} is the vector of design variables, \mathbf{u} is the displacement vector, \mathbf{f} is the fluid state vector (cf. (12) and (13)) and \mathbf{h}/\mathbf{g} are equality/inequality constraints, respectively. The superscripts ‘ u ’ and ‘ d ’ indicate the undeformed and deformed structural configuration. Typical objectives and constraints include pressure drop, drag, flow rate, energy loss, and mass.

6.1 Sensitivity analysis

The following discussion focuses on the sensitivity analysis of the design objective z , but can be applied analogously

to design constraints. The derivative of the objective with respect to the design variables can be written as:

$$\frac{dz}{ds} = \frac{\partial z}{\partial \mathbf{s}} + \left(\frac{\partial z}{\partial \mathbf{u}}\right)^T \frac{d\mathbf{u}}{ds} + \left(\frac{\partial z}{\partial \mathbf{f}}\right)^T \frac{d\mathbf{f}}{ds}. \quad (18)$$

The derivative of the displacements with respect to the design variables is computed from the derivative of the structural residual equation (11):

$$\frac{d\mathbf{R}_S}{ds} = \frac{\partial \mathbf{R}_S}{\partial \mathbf{s}} + \frac{\partial \mathbf{R}_S}{\partial \mathbf{u}} \frac{d\mathbf{u}}{ds} = \mathbf{0}. \quad (19)$$

Solving (19) for $d\mathbf{u}/ds$ yields:

$$\frac{d\mathbf{u}}{ds} = -\underbrace{\left(\frac{\partial \mathbf{R}_S}{\partial \mathbf{u}}\right)^{-1}}_{\mathbf{K}_T} \frac{\partial \mathbf{R}_S}{\partial \mathbf{s}} = -\mathbf{K}_T^{-1} \left(\frac{\partial \mathbf{f}_S^{int}}{\partial \mathbf{s}} + \frac{\partial \mathbf{f}_S^k}{\partial \mathbf{s}} - \underbrace{\frac{\partial \mathbf{f}_S^{ext}}{\partial \mathbf{s}}}_{=0} \right), \quad (20)$$

where \mathbf{K}_T is the tangential stiffness matrix. Assuming that the external forces do not depend on the design variables, the term $\partial \mathbf{f}_S^{ext} / \partial \mathbf{s}$ vanishes. The partial derivative of the

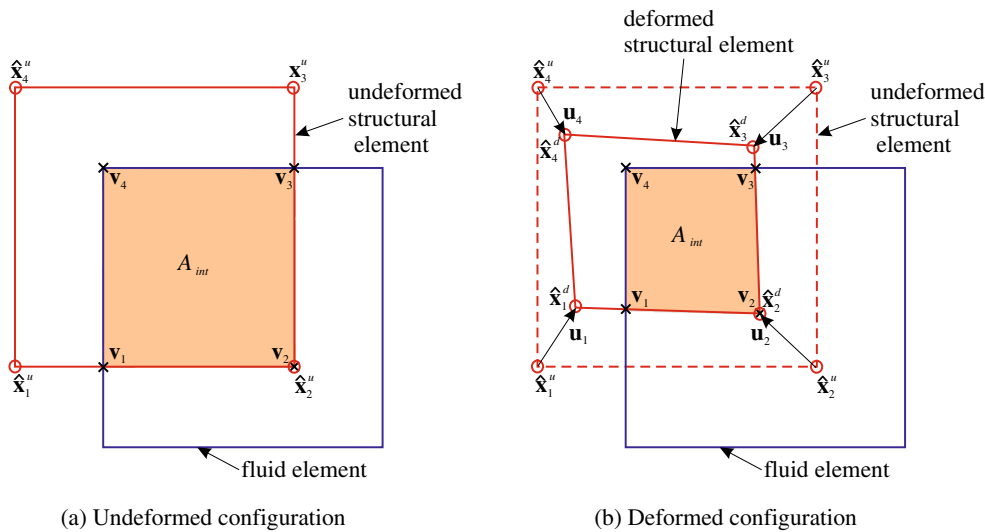


Fig. 7 Intersection of structure and fluid mesh

internal force with respect to the design variables, $\partial \mathbf{f}_S^{int} / \partial \mathbf{s}$, is computed as (cp. (9)):

$$\begin{aligned} \frac{\partial \mathbf{f}_S^{int}}{\partial \mathbf{s}} &= \left[\frac{\partial \mathbf{f}_S^{int}}{\partial \mathbf{s}_m}, \frac{\partial \mathbf{f}_S^{int}}{\partial \mathbf{s}_t}, \frac{\partial \mathbf{f}_S^{int}}{\partial \mathbf{s}_s}, \frac{\partial \mathbf{f}_S^{int}}{\partial \mathbf{s}_e} \right] \\ &= \left[\int_A \mathbf{B}^T \frac{\partial \mathbf{P}}{\partial \mathbf{s}_m} \mathbf{t} dA, \int_A \mathbf{B}^T \left(\frac{\partial \mathbf{P}}{\partial \mathbf{s}_t} \mathbf{t} + \mathbf{P} \frac{\partial \mathbf{t}}{\partial \mathbf{s}_t} \right) dA, \right. \\ &\quad \left. \mathbf{0}, \int_A \mathbf{B}^T \frac{\partial \mathbf{P}}{\partial \mathbf{s}_e} \mathbf{t} dA \right]. \end{aligned} \tag{21}$$

For the term $\partial \mathbf{f}_S^k / \partial \mathbf{s}$ only the derivative with respect to the support design variables, \mathbf{s}_s , does not vanish (cp. (10)):

$$\frac{\partial \mathbf{f}_S^k}{\partial \mathbf{s}_s} = \frac{\partial \mathbf{K}_S}{\partial \mathbf{s}_s} \mathbf{u}, \tag{22}$$

where \mathbf{K}_S is the global support-stiffness matrix.

Owing to the large number of optimization variables needed to resolve the geometry via a material distribution

Table 2 Parameters for the interpolated quantities

Parameter	Value
Maximum Young's modulus of center layer (E_C^{max})	$5 \cdot 10^8$
Young's modulus of structural layers (E_S)	$5 \cdot 10^{10}$
Thickness of center layer (t_C)	0.5
Minimum thickness of structural layer (t_S^{min})	0.1
Maximum thickness of structural layer (t_S^{max})	2
Exponent for support stiffness interpolation (n_s)	3
Minimum support stiffness (k_s^{min})	$1 \cdot 10^{-4}$
Maximum support stiffness (k_s^{max})	$1 \cdot 10^{10}$
Maximum eigenstrain (ϵ_e^{max})	0.1

approach, we solve the above optimization problem using gradient based methods and compute the design sensitivities via an adjoint approach.

The derivative of the fluid state with respect to the design variables, $d\mathbf{f}/d\mathbf{s}$, is computed from the fluid residual equation (15):

$$\frac{d\mathbf{R}_F}{d\mathbf{s}} = \frac{\partial \mathbf{R}_F}{\partial \mathbf{s}} + \frac{\partial \mathbf{R}_F}{\partial \mathbf{f}} \frac{d\mathbf{f}}{d\mathbf{s}} + \frac{\partial \mathbf{R}_F}{\partial \mathbf{u}} \frac{d\mathbf{u}}{d\mathbf{s}} = 0. \tag{23}$$

Substituting (20) into (23) yields:

$$\begin{aligned} \frac{d\mathbf{f}}{d\mathbf{s}} &= - \underbrace{\left(\frac{\partial \mathbf{R}_F}{\partial \mathbf{f}} \right)^{-1}}_{\mathbf{J}_F} \left(\frac{\partial \mathbf{R}_F}{\partial \mathbf{s}} - \frac{\partial \mathbf{R}_F}{\partial \mathbf{u}} \mathbf{K}_T^{-1} \left(\frac{\partial \mathbf{f}_S^{int}}{\partial \mathbf{s}} + \frac{\partial \mathbf{f}_S^k}{\partial \mathbf{s}} \right) \right) \\ &\quad \text{with } \mathbf{p} = \mathbf{p}(\mathbf{u}, \mathbf{s}), \\ &= -\mathbf{J}_F^{-1} \frac{\partial \mathbf{R}_F}{\partial \mathbf{p}} \left(\frac{\partial \mathbf{p}}{\partial \mathbf{s}} - \frac{\partial \mathbf{p}}{\partial \mathbf{u}} \mathbf{K}_T^{-1} \left(\frac{\partial \mathbf{f}_S^{int}}{\partial \mathbf{s}} + \frac{\partial \mathbf{f}_S^k}{\partial \mathbf{s}} \right) \right), \end{aligned} \tag{24}$$

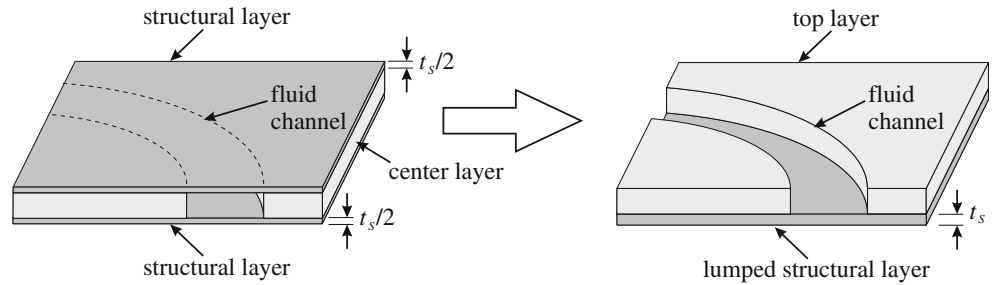
where the matrix \mathbf{J}_F is the Jacobian of the fluid problem and the vector \mathbf{p} defines the impermeabilities. Due to the large number of design variables, we employ the adjoint method in the following. Substituting (20) and (24) into the sensitivity equation (18) results in:

$$\begin{aligned} \frac{dz}{d\mathbf{s}} &= \frac{\partial z}{\partial \mathbf{s}} - \left(\frac{\partial z}{\partial \mathbf{u}} \right)^T \mathbf{K}_T^{-1} \left(\frac{\partial \mathbf{f}_S^{int}}{\partial \mathbf{s}} + \frac{\partial \mathbf{f}_S^k}{\partial \mathbf{s}} \right) \\ &\quad - \mathbf{a}_1 \times \frac{\partial \mathbf{R}_F}{\partial \mathbf{p}} \left(\frac{\partial \mathbf{p}}{\partial \mathbf{s}} + \frac{\partial \mathbf{p}}{\partial \mathbf{u}} \mathbf{K}_T^{-1} \left(\frac{\partial \mathbf{f}_S^{int}}{\partial \mathbf{s}} + \frac{\partial \mathbf{f}_S^k}{\partial \mathbf{s}} \right) \right), \end{aligned} \tag{25}$$

where \mathbf{a}_1 is the solution of the following adjoint equation:

$$\mathbf{a}_1 = \left(\frac{dz}{d\mathbf{f}} \right)^T \mathbf{J}_F^{-1}. \tag{26}$$

Fig. 8 Lumping two structural layers into one



The evaluation of $\partial \mathbf{R}_F / \partial \mathbf{p}$ and $dz/d\mathbf{f}$ in (25) and (26) has been described in Pingen et al. (2009a), the partial derivatives of the impermeabilities, $\partial \mathbf{p} / \partial \mathbf{s}$ and $\partial \mathbf{p} / \partial \mathbf{u}$, are discussed in Section 6.1.1. Rearranging (25) we get:

$$\frac{dz}{ds} = \frac{\partial z}{\partial \mathbf{s}} - \mathbf{a}_1 \frac{\partial \mathbf{R}_F}{\partial \mathbf{p}} \frac{\partial \mathbf{p}}{\partial \mathbf{s}} + \mathbf{a}_2 \left(\frac{\partial \mathbf{f}_S^{int}}{\partial \mathbf{s}} + \frac{\partial \mathbf{f}_S^k}{\partial \mathbf{s}} \right), \quad (27)$$

where \mathbf{a}_2 is the solution to the second adjoint problem defined by:

$$\mathbf{a}_2 = \left(\mathbf{a}_1 \frac{\partial \mathbf{R}_F}{\partial \mathbf{p}} \frac{\partial \mathbf{p}}{\partial \mathbf{u}} - \left(\frac{\partial z}{\partial \mathbf{u}} \right)^T \right) \mathbf{K}_T^{-1}. \quad (28)$$

In the current study we do not consider objectives that depend directly on the design variables or the displacements. Therefore, the terms $\partial z / \partial \mathbf{s}$ in (27) and $\partial z / \partial \mathbf{u}$ in (28) vanish.

6.1.1 Sensitivities of the fluid porosities

As outlined in (16), the impermeabilities depend explicitly on variations in the structural density distribution, ρ^i , and the structural deformations, as the displacements \mathbf{u} affect the intersection areas A_{int}^{ij} . The derivative of the

impermeabilities with respect to the design variables is given by:

$$\frac{\partial p^j}{\partial s^i} = \begin{cases} \frac{A_{int}^{ij}}{A_F^j \rho^{solid}} \frac{d\rho^i}{ds^i} & \text{if } j\text{-th fluid element} \\ & \text{and } i\text{-th structural} \\ & \text{element intersect,} \\ 0 & \text{otherwise,} \end{cases} \quad (29)$$

where for the term $d\rho^i/ds^i$ only the derivatives with respect to the material design variables, s_m^i , do not vanish:

$$\frac{d\rho^i}{ds_m^i} = \rho^{solid}. \quad (30)$$

The derivative of the impermeability with respect to the displacements is defined as follows:

$$\frac{\partial p^j}{\partial \mathbf{u}^i} = \begin{cases} \frac{\rho^i}{A_F^j \rho^{solid}} \frac{dA_{int}^{ij}}{d\mathbf{u}^i} & \text{if } j\text{-th fluid element} \\ & \text{and } i\text{-th structural} \\ & \text{element intersect,} \\ 0 & \text{otherwise.} \end{cases} \quad (31)$$

Fig. 9 Boundary conditions for the three-port manifold

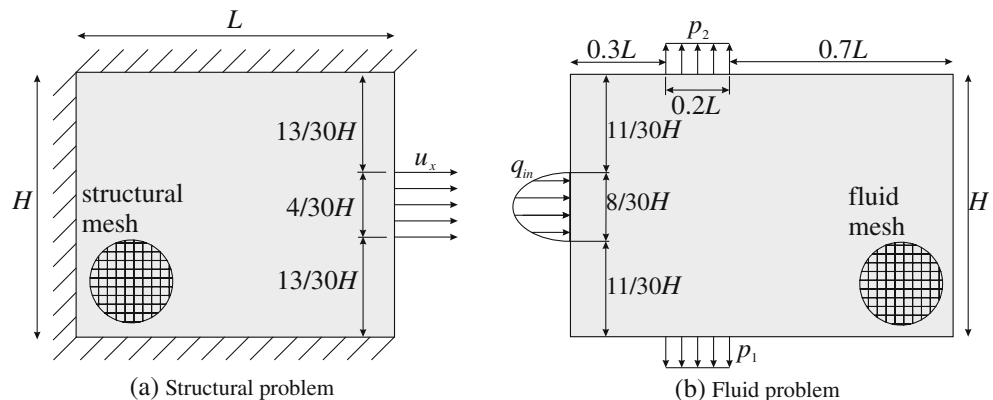
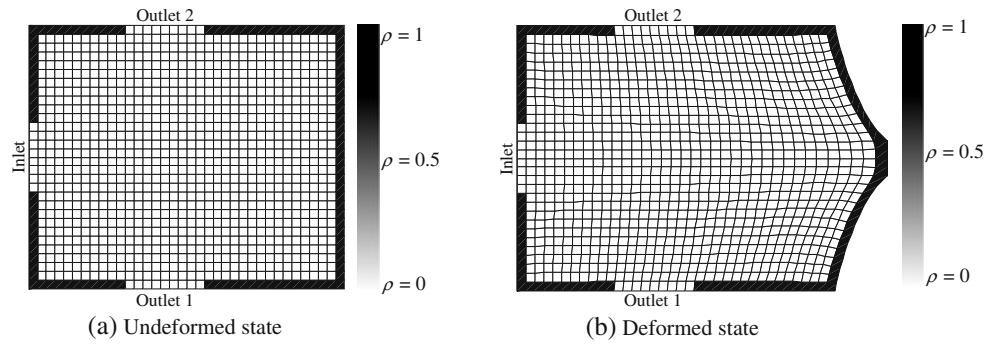


Fig. 10 Initial structural density distribution for the three-port manifold



The term $dA_{int}^{ij}/d\mathbf{u}^i$ can be expanded in the following way (cp. Fig. 7):

$$\frac{dA_{int}^{ij}}{d\mathbf{u}^i} = \underbrace{\frac{dA_{int}^{ij}}{d\mathbf{v}_k}}_{T_1} \underbrace{\frac{d\mathbf{v}_k}{d\hat{\mathbf{x}}_l}}_{T_2} \underbrace{\frac{d\hat{\mathbf{x}}_l}{d\mathbf{u}^i}}_{T_3}, \tag{32}$$

where T_1 defines the dependency of the intersection area A_{int}^{ij} on the vertices \mathbf{v}_k of the polygon determining A_{int}^{ij} ; T_2 characterizes the dependency of the polygon vertices on the position of the structural nodes $\hat{\mathbf{x}}_l$; T_3 describes the dependency of the nodes $\hat{\mathbf{x}}_l$ on the displacements \mathbf{u}^i of the i -th structural element. Due to the definition of $\hat{\mathbf{x}}_l$, T_3 is simply a unity matrix in the deformed case and a zero-matrix in the undeformed case, respectively.

The adjoint sensitivity analysis has been validated through comparison with finite difference results.

7 Numerical examples

To illustrate the utility of the current approach we study the design of three tunable manifolds. The optimization problems are solved by the Globally-Convergent Method of Moving Asymptotes (GCMMA) of Svanberg (1995).

At each iteration in the optimization process we first solve the structural equilibrium equations for the deformed configuration. Then both, undeformed and deformed, material distributions are mapped onto the fluid mesh, leading to an undeformed and deformed fluid impermeability

Table 3 Objectives for the three-port manifold problem

Structural state	Outlet 1	Outlet 2
Undeformed	Maximize the mass flow, q_1^u	Minimize the mass flow, q_2^u
Deformed	Minimize the mass flow, q_1^d	Maximize the mass flow, q_2^d

distribution. The flow solutions for both impermeability distributions are computed by advancing the flow in time until steady state convergence. The design criteria in the undeformed and deformed configurations are evaluated to obtain values of the objective function and constraints. The sensitivities are evaluated by the adjoint method using a direct solver for the linear systems, (26) and (28). The

Table 4 Parameters for the three-port manifold

Parameter type	Parameter	Value
Physical	Length (L)	36
	Height (H)	30
	Reynolds number (RE)	10
	Critical length (L_c)	9
	Dimensionless relaxation time (τ)	1/1.9
	Viscosity (ν_F)	$\frac{1}{6} (2\tau - 1)$
	Inlet velocity (v_{in})	$RE \cdot \nu_F / L_c$
	Outlet pressure (p_{out})	1/3
	Prescribed external displacement (u_x)	$L/6$
	Poisson ratio (ν)	0.4
Discretization	Fluid-domain mesh ($n_x \times n_y$)	45×31
	Fluid-domain grid size	$L/(n_x - 1)$
	Structural-domain mesh ($m_x \times m_y$)	37×31
	Structural-domain grid size	$L/(m_x - 1)$
Algorithmic	Lower, upper limit for s^i (s^{min}, s^{max})	0, 1
	Step size (Δs)	$0.1(s^{max} - s^{min})$
	Number of GCMMA subcycles	2
Convergence	Tolerance for KKT conditions (ϵ_{kkt})	$1 \cdot 10^{-2}$
	Tolerance for design change (ϵ_s)	$2 \cdot 10^{-4}$
	Tolerance for constraint violation (ϵ_c)	$5 \cdot 10^{-3}$

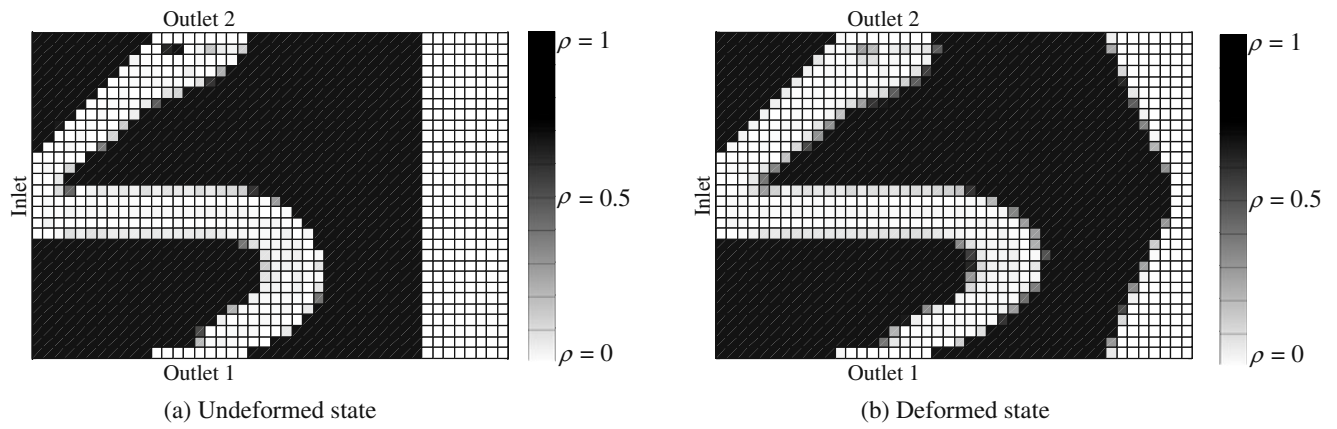


Fig. 11 Optimized impermeability distribution for the three-port manifold

convergence of the optimization process is monitored via the residual of the Karush–Kuhn–Tucker conditions \mathbf{R}_{kkt} , the design change $\|\Delta\mathbf{s}\|$, and the constraint violations. The following convergence criteria are defined:

$$\|\mathbf{R}_{kkt}\| < \epsilon_{kkt} \|\mathbf{R}_{kkt}\|_0, \tag{33}$$

$$\|\Delta\mathbf{s}\| < \epsilon_s N_s, \tag{34}$$

$$g_j < \epsilon_c, \tag{35}$$

where $\|\mathbf{R}_{kkt}\|_0$ is the norm of the residual of the initial design and N_s is the number of optimization variables. The tolerances ϵ_{kkt} , ϵ_s and ϵ_c for the three examples are defined in Tables 4, 8, and 9. For all three examples, we use the same interpolations linking abstract and physical design variables. The interpolation parameters are listed in Table 2. All values related to the flow solution in the following examples are in dimensionless lattice-units.

Using a 2-D approximation for the structural response and the flow allows us to simplify the three-layer model and lump the two structural layers into one. For this simplified model the center layer that houses the fluid channels becomes the top layer, which is connected to a single lumped structural layer. Figure 8 illustrates this simplified model.

7.1 Three-port manifold

In the first example, we consider a manifold that routes the flow from one inlet into two outlet ports. The goal of the design problem is to find the layout of the fluid channels and the thickness distribution of the structural layers such that the mass flow through the outlet ports can be controlled through an elastic deformation in response to a prescribed external displacement. In this example, internal actuation via eigenstrains is not considered and the supports are not altered in the optimization process. The boundary

conditions for both the structural and the fluid problems are depicted in Fig. 9. The gridded circles illustrate the structural and fluid mesh, respectively. The structure is clamped along all edges except for the right one. The center of the latter is subjected to horizontal displacements $u_x = L/6$. The boundary conditions for the fluid model, Fig. 9b, are a parabolic inlet velocity distribution and a prescribed static pressure at both outlets. Note, that the fluid domain is 20% longer than the structural mesh. This ensures that the fixed fluid mesh covers the entire structural domain when the structure expands during deformation.

The initial density distributions in the undeformed and deformed configuration are illustrated in Fig. 10. We initialize the density distribution with $\rho = 1$ at the boundaries that are neither inlet nor outlet and $\rho = 0$ elsewhere. The thickness of the structural layer is uniformly initialized with $s_i^i = 0.5 \forall i$.

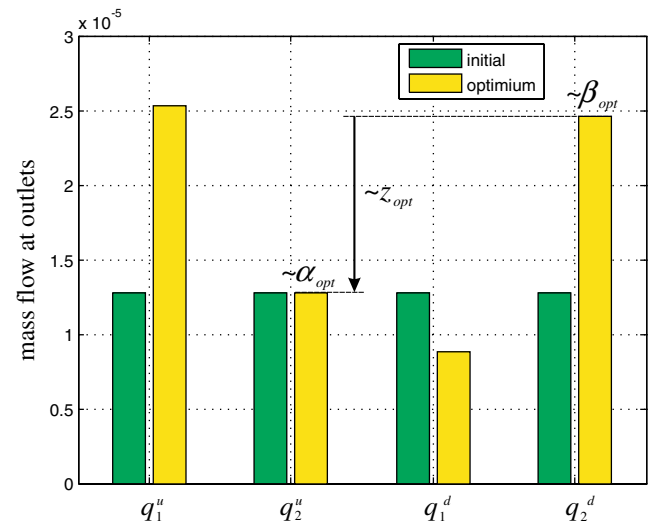


Fig. 12 Comparison between initial and optimized dynamic pressures at outlet 1 and 2 for the three-port manifold

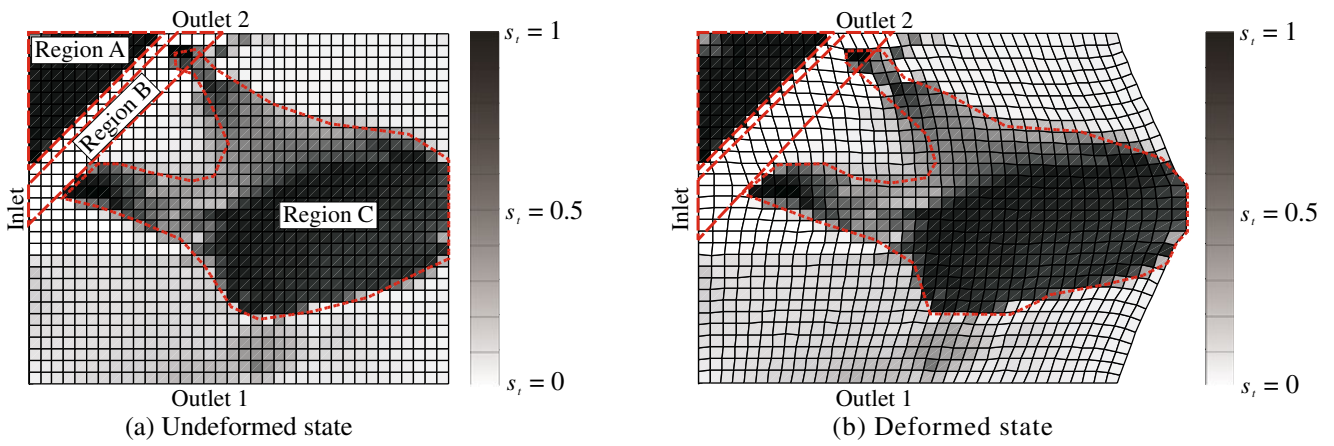


Fig. 13 Optimized relative thickness of structural layer for the three-port manifold

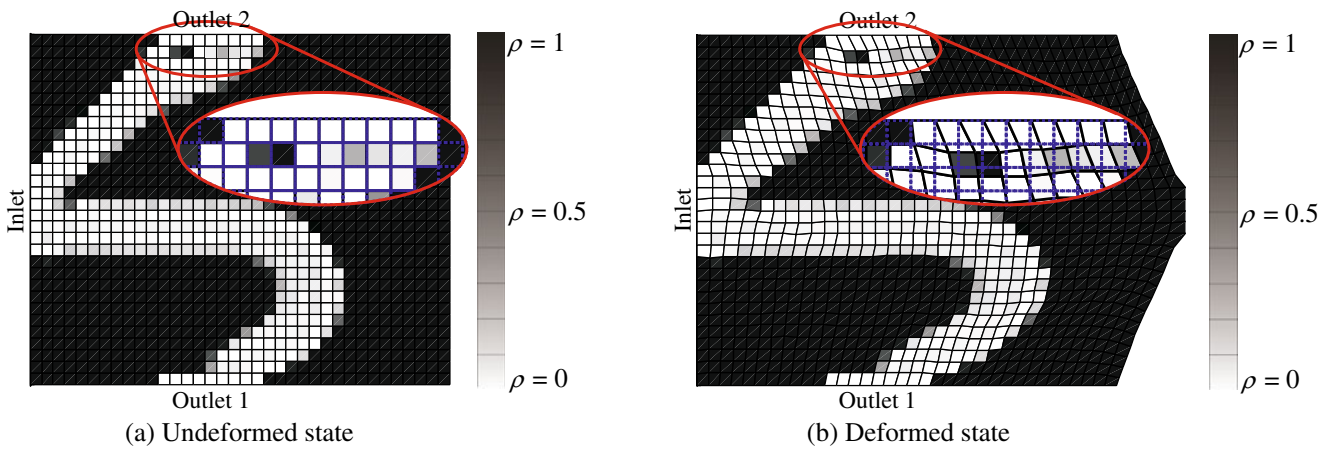


Fig. 14 Smearing effects due to mismatching meshes (Eulerian fluid mesh on Lagrangian density distribution)

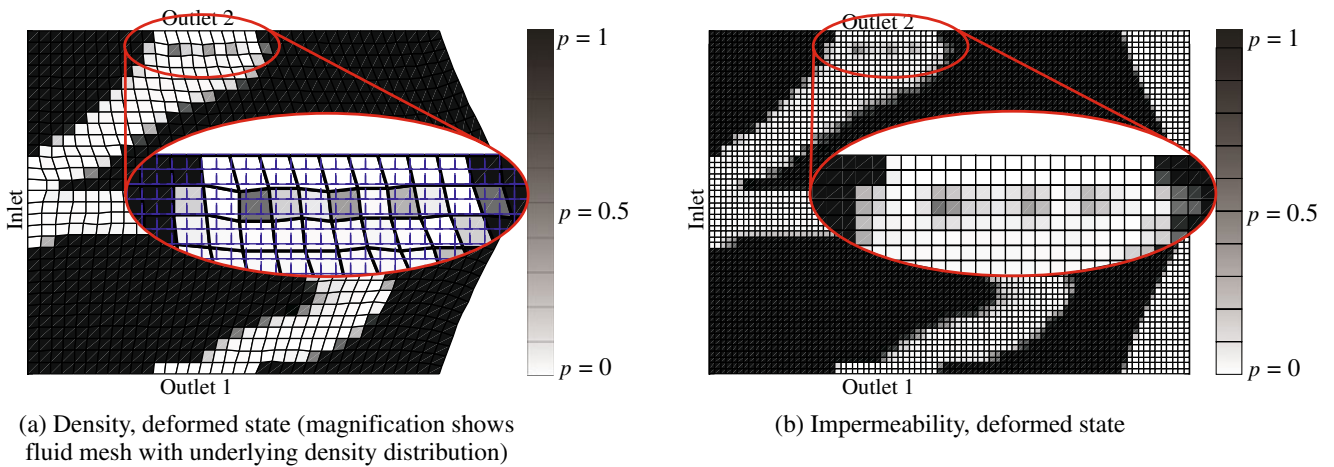


Fig. 15 Material layout after 274 iterations for refined fluid mesh

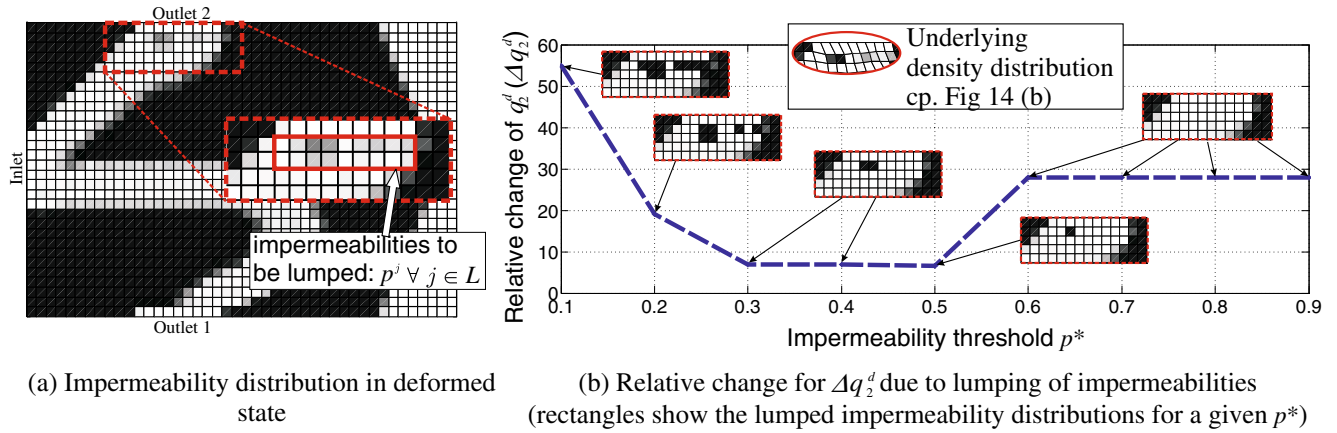


Fig. 16 Lumping of intermediate impermeabilities and its effect

The design of a tunable manifold is formulated as a multi-criteria optimization problem. The goal is to find the layout of a flow-switch that guides the flow to one outlet in the undeformed configuration and to a second outlet in the deformed configuration. Specifically, the objective is to maximize the mass flow at the lower outlet in the undeformed state and minimize it in the deformed configuration. For the outlet at the top the goal is opposite: minimize the mass flow in the undeformed state and maximize it in the deformed configuration. These four objectives are listed in Table 3. The multiple objectives are treated via a bound formulation (Stadler 1988), which seeks a compromise between all objectives while avoiding that one objective is improved whereas another objective deteriorates significantly. The optimization problem can be written as follows:

$$\begin{aligned}
 \min_s \quad & z = \alpha - \beta, \\
 \text{s.t.} \quad & g_1 = q_1^u - \beta \geq 0, \\
 & g_2 = \alpha - q_2^u \geq 0, \\
 & g_3 = \alpha - q_1^d \geq 0, \\
 & g_4 = q_2^d - \beta \geq 0, \\
 & g_5 = 1.005 - \frac{(p_{in})^u}{(p_{in}^0)^u} \geq 0, \\
 & g_6 = 1.005 - \frac{(p_{in})^d}{(p_{in}^0)^d} \geq 0, \\
 & g_7 = \frac{1}{N_e} \sum_i^{N_e} \frac{\rho^i}{\rho^{solid}} - 0.75 \geq 0, \\
 & s_m^{min} \leq s_m^i \leq s_m^{max}, \\
 & s_t^{min} \leq s_t^i \leq s_t^{max}.
 \end{aligned} \tag{36}$$

where α and β are auxiliary variables. The mass flow is denoted by q . The subscripts indicate the outlet ports: ‘1’

for the lower port and ‘2’ for the upper port. The superscripts ‘u’ and ‘d’ refer to the undeformed and deformed configurations. The constraints g_5, g_6 ensure that the total inlet pressure is equal or less than 100.5% of the inlet pressure of the initial design (cf. Fig. 10). The mass constraint g_7 requires that at least 75% of the design domain is solid where N_e is the number of structural elements. The parameters for the three-port manifold example are summarized in Table 4. Due to the structure of (36), at every locally optimal solution the following equalities are satisfied:

$$\alpha = \max(q_2^u, q_1^d), \tag{37}$$

$$\beta = \min(q_1^u, q_2^d), \tag{38}$$

The optimization process converged in 418 iterations. While the thickness distribution converged rather fast, the density distribution showed a much slower convergence rate and hence required a large number of optimization steps. Figure 11 shows the optimized fluid channel. In the undeformed configuration, the bulk of the fluid flows through the lower outlet, as this flow path has a smaller pressure drop than the flow path to the upper port. In the deformed configuration the channel to the lower outlet port is stretched significantly. The additional length and curvature increases the pressure drop of the lower channel,

Table 5 Flow rates and objective for design with and without plug (cp. (37) and (38))

	With island	Without island
q_1^u	2.58×10^{-5}	$2.33 \times 10^{-5} \approx \beta$
q_2^u	$1.27 \times 10^{-5} \approx \alpha$	$1.74 \times 10^{-5} \approx \alpha$
q_1^d	9.34×10^{-6}	7.79×10^{-6}
q_2^d	$2.48 \times 10^{-5} \approx \beta$	3.15×10^{-5}
$z = \alpha - \beta$	-1.21×10^{-5}	-0.59×10^{-5}

Table 6 Norm of fluid forces, relative errors for solution with and without fluid forces

Norm of fluid forces	$\ \mathbf{f}_L^u\ = 9.3 \cdot 10^{-3}$
Relative error in displacements	$e_u = 3.7 \cdot 10^{-12}\%$
Relative error in impermeabilities	$e_p = 1.7 \cdot 10^{-12}\%$
Relative error in dynamic pressure	$e_z = -1.7 \cdot 10^{-9}\%$

reducing the mass flow, q_1^d , at the lower outlet. Moreover, Fig. 11b illustrates that the channel to the upper outlet widens under the structural deformation, increasing q_2^d .

A quantitative comparison between initial and optimized mass flows is shown in Fig. 12: three of the four mass flow rates are improved significantly compared to the initial design (cf. Table 3). However, the mass flow through the upper outlet in the undeformed configuration, q_2^u , hardly changed during the optimization.

Figure 13 displays the relative thickness of the structural layer. It shows that there are two regions in which the thickness of the structural layer is maximized, resulting in a stiffening of the corresponding structure. One is in the top left corner of the design domain (Region A), effectively stiffening the left edge of the channel to outlet 2. The region of the channel to outlet 2 (Region B) on the other hand has a minimum thickness. This thickness layout amplifies the widening of the channel to outlet 2 under deformation. The second region of high thickness values (Region C) connects the point of load incidence with the apex of the channel to outlet 1. Since the lower left of the design domain is weakened, this allows to further increase the length and curvature of this channel.

7.1.1 Influence of small features on the performance

The undeformed material distribution shows a small solid feature in front of the upper outlet, Fig. 11a. In the deformed configuration this feature is stretched. However, in the fluid model, the stretched feature is represented by intermediate impermeabilities. This brings up two questions: (I) is this feature an artifact that occurs owing to the chosen numerical representation? and (II) what are its benefits?

To answer (I) the mapping procedure is examined: in the undeformed configuration, the fluid and solid meshes are almost aligned, resulting in a mapping $p^j \approx \rho^i$, which leads to a mostly black and white impermeability distribution, see Fig. 11a. However, as the structure stretches, the Lagrangian solid mesh deforms while the Eulerian fluid mesh stays fixed, leading to a mismatch between the two meshes. This results in smeared-out and thus lower interface impermeabilities in the deformed state, Fig. 11b. Figure 14 illustrates this issue. The magnification depicts the density distribution on the Lagrangian mesh overlaid with the Eulerian fluid mesh. Figure 11b shows that in the deformed case two ‘solid’ densities, i.e. $\rho \approx 1$, get distributed over six fluid elements, hence the smearing.

In order to mitigate the smearing effect, the same problem was optimized using a twice as fine fluid mesh. Figure 15 shows both the density as well as the impermeability distribution for the refined fluid mesh after 274 iterations. As can be seen from Fig. 15, the finer fluid mesh effectively reduces the smearing effect, but does not prevent the formation of a solid feature in front of outlet 2.

To analyze the effect of the smeared out impermeabilities in the deformed configuration we lumped the intermediate impermeabilities into a discrete 0–1 distribution which is shown in Fig. 16. The intermediate impermeability distribution in Fig. 16a is compared with a lumped one, where the values for lumped impermeabilities, p_l , are obtained from the following:

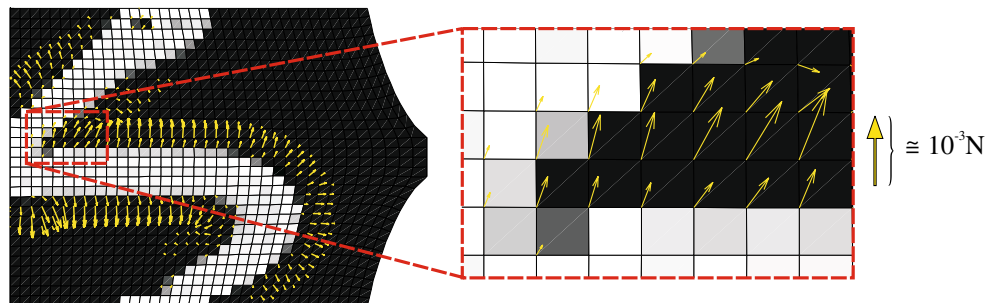
$$p_l^j = \begin{cases} 0 & \text{if } p^j \leq p^* \quad \forall j \in L, \\ 1 & \text{if } p^j > p^* \quad \forall j \in L, \\ p^j & \quad \forall j \notin L, \end{cases} \tag{39}$$

where L is the list of 18 elements to be lumped. The relative change of the flow rate, Δq_2^d due to the lumping is defined as:

$$\Delta q_2^d = \frac{q_2^d(\mathbf{p}_l) - q_2^d(\mathbf{p})}{q_2^d(\mathbf{p})}, \tag{40}$$

where \mathbf{p} and \mathbf{p}_l define regular and the lumped impermeability distribution, respectively. Figure 16b shows the

Fig. 17 Fluid forces acting of structure \mathbf{f}_L^u



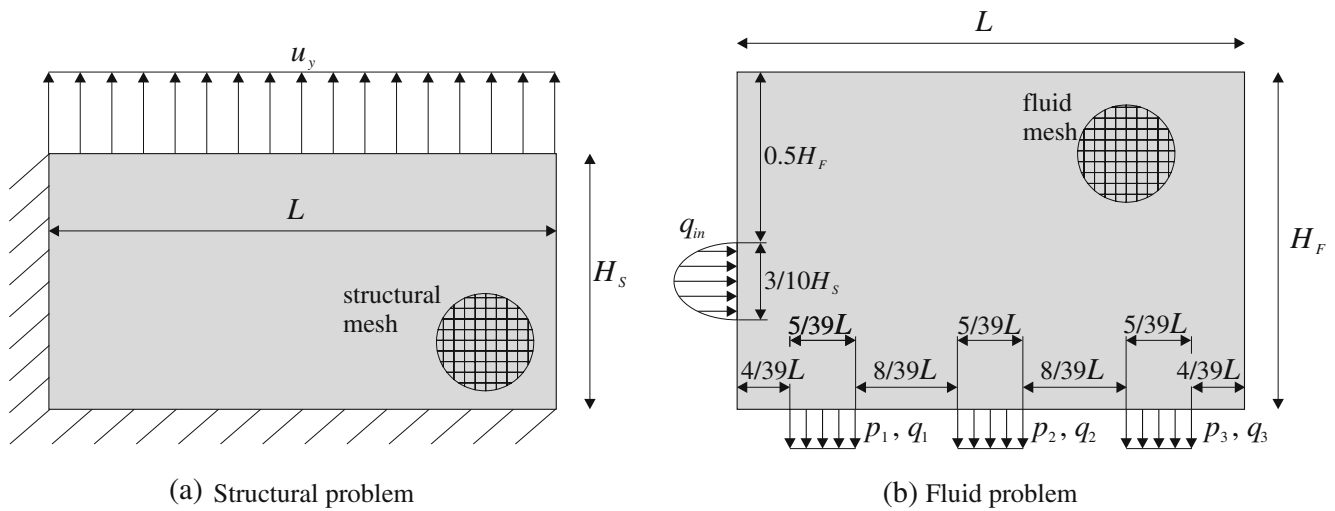


Fig. 18 Boundary conditions for the four-port manifold with external actuation

underlying density distribution (ellipse) as well as the corresponding lumped impermeabilities for different threshold values p^* (rectangles). As can be seen in the figure, an intermediate impermeability threshold of $0.3 \leq p^* \leq 0.5$ leads to a small, $\approx 7\%$, change in the flow rate q_2^d . The lumped impermeability distribution for thresholds $0.3 \leq p^* \leq 0.4$ resemble the underlying densities the closest (two solid elements). Since the smeared impermeability distribution only differs by $\approx 7\%$ from the discrete, and thus physically more meaningful distribution, we conclude that the geometric mapping produces physically consistent flow solutions/results for fluid problems with low Reynolds numbers as considered in this work.

After having demonstrated that the island is not an artifact, we analyze the benefits of this small feature. We compare the results from the original optimized design, as depicted in Fig. 11, with a design where the solid feature is removed, i.e. a lumped impermeability with a threshold of $p^* \geq 0.6$, cp. Fig. 16b. The quantitative results are listed in Table 5. The values show that the design without the island has twice as large of an objective value compared to the one with the island. The reason for this lies in the fact that without island, the flow rate for outlet 2 increases while at the same time the flow rate for outlet 1 decreases. This results in $q_1^u < q_2^d \rightarrow \beta = q_1^u$. Additionally, $\alpha \approx q_2^u$ is increased significantly due to the lower pressure drop when the island is removed. The combination of these effects results in an

overall worsened objective when the feature is not present. This analysis shows that the performance of the optimized topology is due to both the geometry of the flow channels and the feature in front of the upper outlet.

7.1.2 Influence of the fluid forces on the structure

The current study neglects the effect of the fluid forces on the structure, leading to a one-way structure-fluid coupling. In this subsection we demonstrate that the error resulting from this simplification is negligible for problems in which the structural displacements due to the fluid pressure are sufficiently small such that they do not affect the flow. This assumption holds for flows with low velocities and pressures and for bulky structures. As topology optimization methods may lead to slender features that might deform significantly even under low fluid pressures, this assumption needs to be verified for the resulting optimized design.

To analyze the influence of the fluid pressure on the structural deformation, we extend our approach described previously. Following a staggered coupling scheme, we compute the fluid pressure in the fluid model and map it onto the structural model leading to an additional external force term. The resulting structural deformations are imposed onto the fluid model as described in Section 5. To ensure proper convergence to steady state, the staggered scheme is repeated until the relative error in displacements, e_u^k , satisfies the following condition:

$$e_u^k = \frac{\|\mathbf{u}^k - \mathbf{u}^{k-1}\|}{\|\mathbf{u}^k\|} \leq 10^{-11}. \tag{41}$$

where k is the iteration index of the staggered scheme.

Table 7 Constraints for the four-port manifold problem

Structural state	@ Outlet 1	@ Outlet 2	@ Outlet 3
Undeformed	$q_1^u = q_{in}^u/2$	$q_2^u = q_{in}^u/4$	$q_3^u = q_{in}^u/4$
Deformed	$q_1^d = q_{in}^d/3$	$q_2^d = q_{in}^d/3$	$q_3^d = q_{in}^d/3$

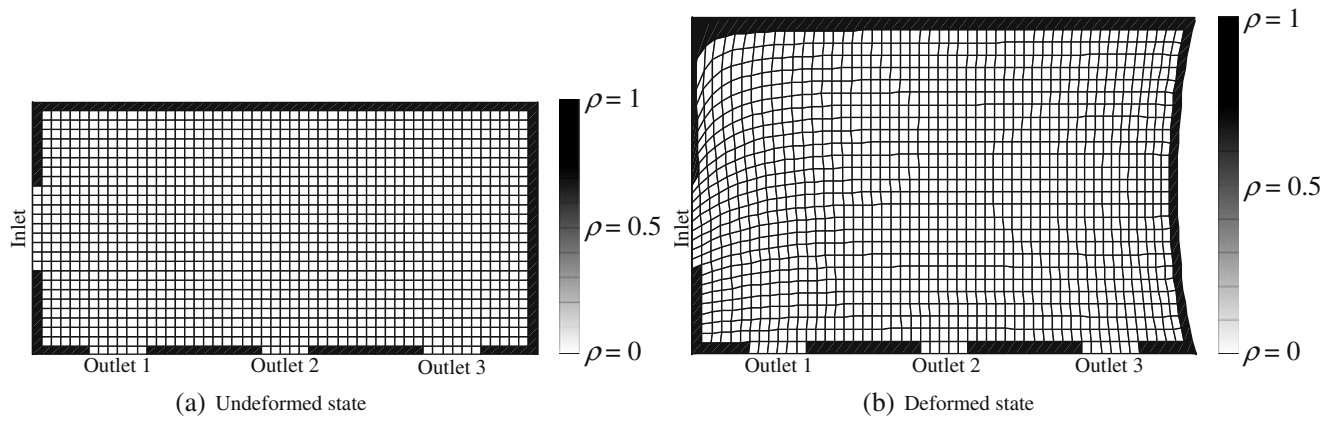


Fig. 19 Initial structural density distribution for the four-port manifold (material and thickness optimization)

Table 6 lists the relative errors of the fluid-structure response when the influence of the fluid forces on the structural deformations is ignored. The relative errors arising from the omission of the fluid forces is negligible as in the present example the fluid forces are insignificant in comparison to the structural stiffness. However, in cases where the structure is more flexible (e.g. long slender components) and/or the fluid velocities are higher, i.e. larger fluid forces, the effect of the fluid pressure on the structure may have to be considered.

Remark 1 The porosity model described in Section 4 can be employed to predict fluid forces \mathbf{f}_E (where the subscript ‘E’ indicates that the force vector is defined on the Eulerian mesh). However, this approach results in forces not only at the fluid–solid interface but also within the solid domain. These non-physical forces occur due to the fact that porous material permits pressure gradients throughout the material. These pressure gradients in the porous material are still allowed to develop when $p = 1$ (solid), thus leading to forces within solid regions. To ensure that fluid forces only occur in the vicinity of the fluid–solid interface a scaled bounce-back boundary method is employed. For details on this method, the reader is referred to the work by Pingen et al. (2006).

Remark 2 Given the fluid forces, \mathbf{f}_E , the mapping described in Section 5 is used to transform \mathbf{f}_E from the Eulerian mesh onto the Lagrangian mesh. This results in a fluid force vector \mathbf{f}_L , where the force acting on the i -th structural element is defined as:

$$f_L^i = \frac{1}{A_i^s} \sum_{j=1}^{n_i} (f_E^j A_{int}^{ji}). \tag{42}$$

This force is equally distributed to the nodes of the i -th structural element, which finally results in the vector of

Table 8 Parameters for the four-port manifold (material and thickness optimization)

Parameter type	Parameter	Value
Physical	Length (L)	48
	Height of fluid domain (H_F)	31
	Height of structural domain (H_S)	24
	Reynolds number (RE)	10
	Critical length (L_c)	9
	Dimensionless relaxation time (τ)	1/1.9
	Viscosity (ν_F)	$\frac{1}{6} (2\tau - 1)$
	Inlet velocity (v_{in})	$RE \cdot \nu_F / L_c$
	Outlet pressure (p_{out})	1/3
	Prescribed external displacement (u_y)	$0.25H_S$
Discretization	Poisson ratio (ν)	0.4
	Fluid-domain mesh ($n_x \times n_y$)	49×32
	Fluid-domain grid size	$L / (n_x - 1)$
	Structural-domain mesh ($m_x \times m_y$)	53×27
	Structural-domain grid size	$L / (m_x - 1)$
Algorithmic	Lower, upper limit for s^i (s^{min}, s^{max})	0, 1
	Step size (Δs)	$0.05(s^{max} - s^{min})$
	Number of GCMMA subcycles	1
Convergence	Tolerance for KKT conditions (ϵ_{kkt})	$1 \cdot 10^{-7}$
	Tolerance for design change (ϵ_s)	$5 \cdot 10^{-3}$
	Tolerance for constraint violation (ϵ_c)	$5 \cdot 10^{-4}$

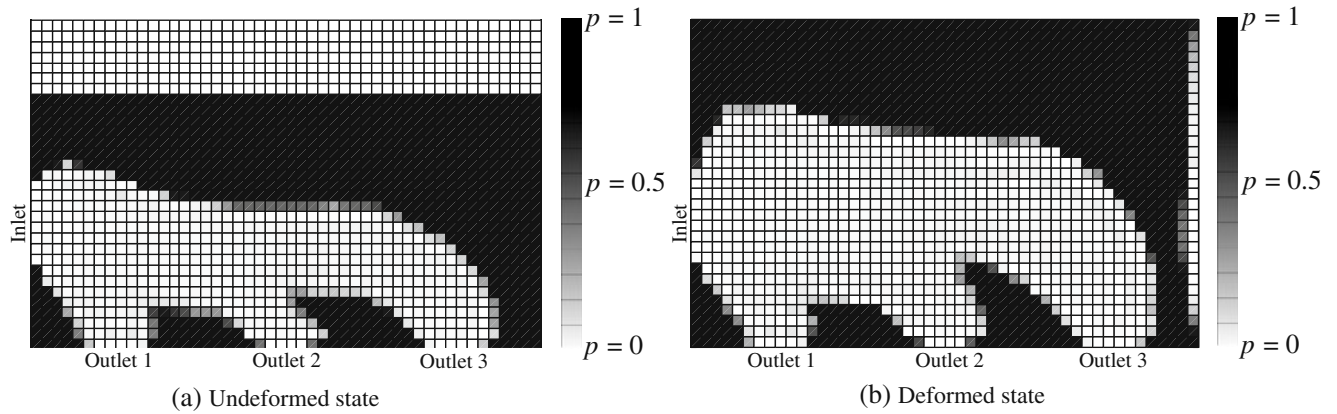


Fig. 20 Optimized impermeability distribution for the four-port manifold with external actuation

nodal fluid forces \mathbf{f}_L^n . This force vector \mathbf{f}_L^n leads to structural deformations. The latter in return affects the intersection areas A_{int}^{ji} (cp. (42)), resulting in slightly different fluid forces f_L^i . Figure 17 shows the fluid forces, \mathbf{f}_L^n , in the structural domain. Note that the forces within the structural solid domain occur due to the mapping in (42).

7.2 Four-port manifold with external actuation

In the second example we optimize a system with one inlet and three outlet ports. As before, the goal of the design problem is to find the layout of the fluid channels and the thickness distribution of the structural layer such that the mass flow through the outlet ports can be controlled through an elastic deformation in response to an external prescribed displacement. Again, internal actuation and varying the support stiffness are not considered. The boundary conditions for both the structural and the fluid problem are depicted in Fig. 18. The gridded circles illustrate the structural and fluid mesh, respectively. The height of the fluid

domain is approximately 25% higher than that of the structural domain. This ensures that the fixed fluid mesh covers the entire structural domain, even when the latter expands during deformation.

We minimize the difference in total pressure between the inlet and the outlets. Furthermore, we require for the undeformed configuration that the flow rate through outlet 1 (q_1^u) is 1/2 of the inlet flow rate, q_{in}^u . The flow rates through the remaining two outlets, q_2^u and q_3^u , are required to be 1/4 of the inlet flow rate. In the deformed configuration all three outlets, q_j^d , for $j = 1, \dots, 3$, should have the same flow rate, i.e. 1/3 of the inlet flow rate in the deformed configuration, q_{in}^d . Table 7 lists the flow rate constraints for the four-port manifold.

The structure is clamped on the left and lower edges. The upper edge is subjected to a prescribed displacement $u_y = 0.25H_S$ in the vertical direction. The boundary conditions for the fluid model, Fig. 18b, are a parabolic inlet velocity and a prescribed static pressure of $p_{out} = 1/3$ at all three outlets.

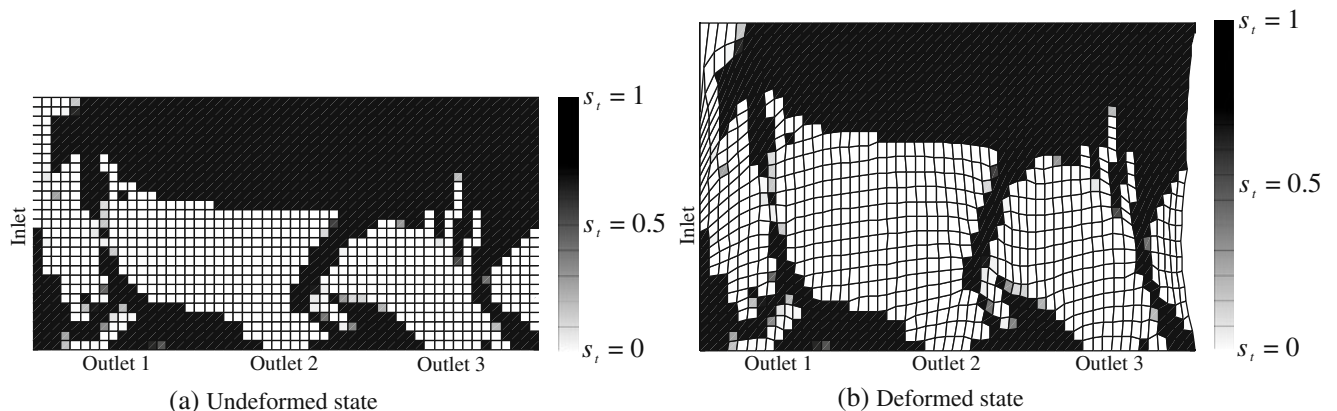


Fig. 21 Optimized relative substrate thickness for the four-port manifold with external actuation

The initial density distributions in the undeformed and deformed configurations are illustrated in Fig. 19. We initialize the density distribution with $\rho = 1$ at the boundary that is neither inlet nor outlet and $\rho = 0$ elsewhere. The substrate thickness is uniformly initialized with $s_t^i = 0.5 \forall i$.

The optimization problem is defined by the following set of equations:

$$\begin{aligned} \min_s z &= p_{in}^u + p_{in}^d - \sum_{j=1}^3 (p_j^u + p_j^d), \\ \text{s.t. } g_1 &= 0.005 - \left(q_{in}^u - \frac{1}{2}q_1^u\right)^2 - \left(q_{in}^d - \frac{1}{4}q_2^d\right)^2 \geq 0, \\ g_2 &= 0.005 - \left(q_{in}^d - \frac{1}{3}q_1^d\right)^2 - \left(q_{in}^u - \frac{1}{3}q_2^u\right)^2 \geq 0, \\ g_3 &= \frac{1}{N_e} \sum_i^{N_e} \frac{\rho^i}{\rho^{solid}} - 0.6 \geq 0, \\ s_m^{min} &\leq s_m^i \leq s_m^{max}, \\ s_t^{min} &\leq s_t^i \leq s_t^{max}, \end{aligned} \tag{43}$$

where, g_1 and g_2 describe the flow rate constraints and g_3 requires that at least 60% of the design domain has to be solid. Table 8 lists the parameters used for the four-port manifold example.

Figure 20 shows the optimized fluid channel, converged after 137 iterations. All three constraints are satisfied. In the undeformed configuration, the mass flow to the output ports 2 and 3 is limited by height of the horizontal main channel. When the structure undergoes deformation, the main channel widens, increasing the mass flow through outlet ports 2 and 3. Furthermore, the fin between outlet 2 and 3 deforms such that the channel to outlet 2 is widened and more flow is directed toward outlet 2. The increased mass flow through outlet 2 and 3 simultaneously leads to a decrease of the mass flow through outlet port 1.

Figure 21 illustrates the optimized relative substrate thickness. The thickness is mostly minimized in areas where the channel is located (cp. Fig. 20). This weakens the structure, allowing for a greater widening of the channel when deformed. The link slightly to the right of the center of the design domain stiffens the connection between the upper half of the design domain and the fin between outlet 2 and 3. When the structure is deformed, this link pulls the tip of the fin up and to the right, redirection the flow.

Table 9 Parameters for the four-port manifold (material, eigenstrain and support-layout optimization)

Parameter type	Parameter	Value	
Physical	Length (L)	48	
	Height of fluid domain (H_F)	24	
	Height of structural domain (H_S)	24	
	Reynolds number (RE)	10	
	Critical length (L_c)	9	
	Dimensionless relaxation time (τ)	1/1.9	
	Viscosity (ν_F)	$\frac{1}{6}(2\tau - 1)$	
	Inlet velocity (v_{in})	$RE \cdot \nu_F / L_c$	
	Outlet pressure (p_{out})	1/3	
	Prescribed external displacement	0	
	Poisson ratio (ν)	0.4	
	Discretization	Fluid-domain mesh ($n_x \times n_y$)	49×25
		Fluid-domain grid size	$L/(n_x - 1)$
Structural-domain mesh ($m_x \times m_y$)		53×27	
Structural-domain grid size		$L/(m_x - 1)$	
Algorithmic	Lower, upper limit for s_m^i, s_s^i (s^{min}, s^{max})	0, 1	
	Lower, upper limit for s_e^i (s_e^{min}, s_e^{max})	-1, 1	
	Step size (Δs)	$0.05(s^{max} - s^{min})$	
	Number of GCMMA subcycles	1	
Convergence	Tolerance for KKT conditions (ϵ_{kkt})	$1 \cdot 10^{-5}$	
	Tolerance for design change (ϵ_s)	$1 \cdot 10^{-2}$	
	Tolerance for constraint violation (ϵ_c)	$1 \cdot 10^{-5}$	

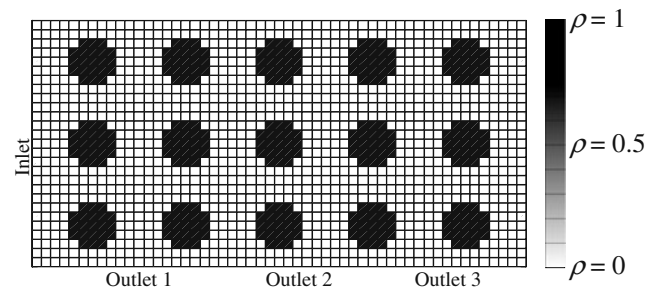


Fig. 22 Initial structural density distribution for the four-port manifold (material with internal actuation)

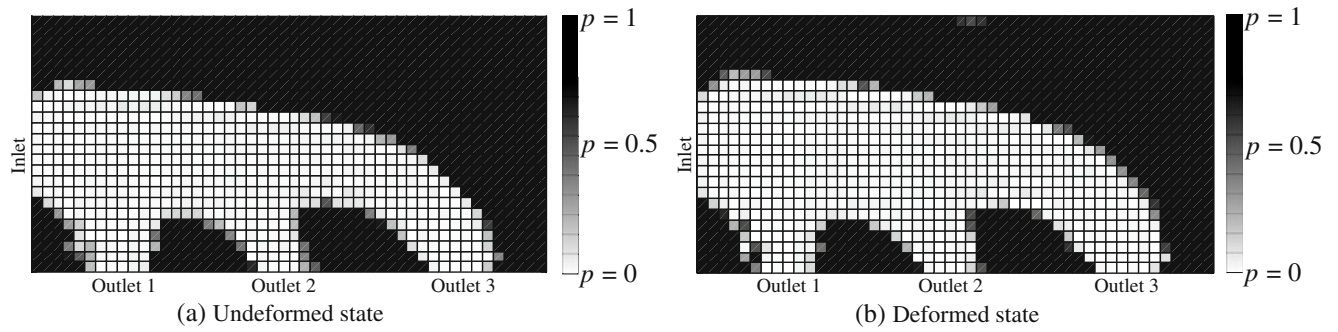


Fig. 23 Optimized impermeability distribution for the four-port manifold with internal actuation

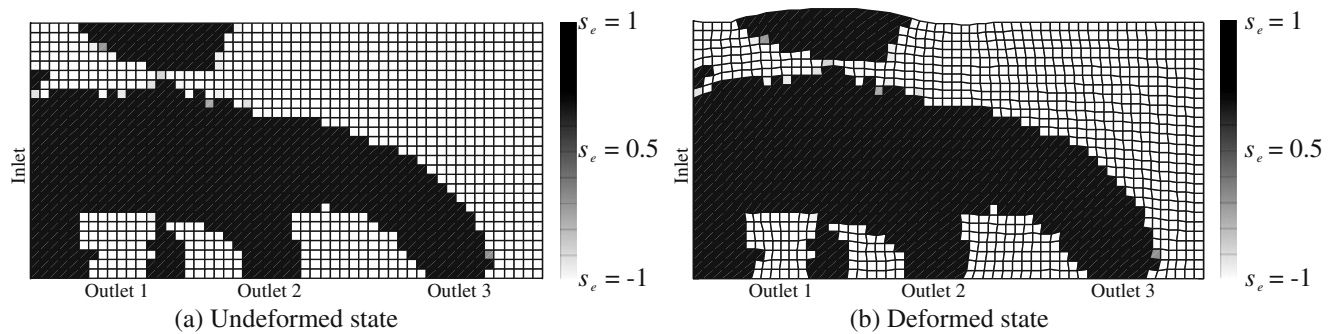


Fig. 24 Optimized eigenstrain for the four-port manifold with internal actuation

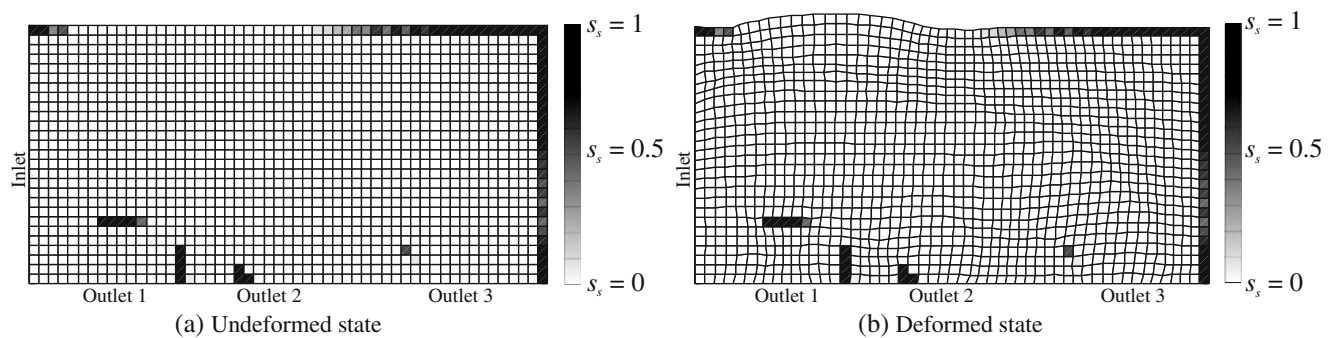


Fig. 25 Optimized support layout for the four-port manifold with internal actuation

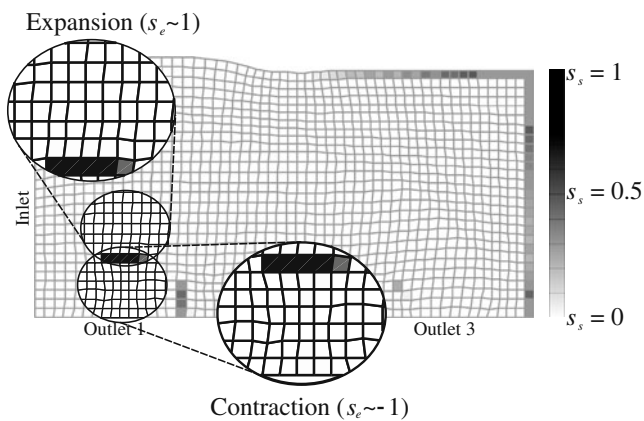


Fig. 26 Detail of optimized support layout in deformed configuration (cf. Figs. 24b and 25b)

7.3 Four-port manifold with internal actuation

The third example considers the same problem as in Section 7.2. However in this example we consider internal instead of external actuation and vary the eigenstrain distribution along with the support stiffness. The thickness is not altered. When employing eigenstrains, an adjustable support-layout is crucial to achieve large local deformations without requiring excessive eigenstrains. Since the system is no longer subjected to an external displacement and the displacements along the structural design domain are fixed, the dimensions of the fluid mesh are chosen such that they match the structural mesh. Table 9 lists the algorithmic parameters. To demonstrate the robustness of the current approach with respect to the initial design, we choose a different initialization for the density distribution, depicted in Fig. 22. The optimization problem is identical to the one defined in (43), but with box constraints on s_e^i and s_s^i instead of s_t^i . The eigenstrain design variables are uniformly initialized with $s_e^i = 10^{-4}$ and the support design with $s_s^i = 0.3$. The substrate thickness is fixed at $t = 1.05$, i.e. $s_t^i = 0.5$.

Figure 23 shows the optimized impermeability distribution after 179 iterations (converged) in the undeformed and deformed configuration. As can be seen from these figures, the channels to the outlet ports 2 and 3 (center and right) expand significantly in the deformed configuration, increasing the flow rates through these ports. On the other hand the channel to outlet port 1 contracts, which reduces the flow for outlet 1. The optimized eigenstrain distribution is illustrated in Fig. 24. It shows positive strains ($s_e^i = 1$: expansion) along the channels to the outlet ports 2 and 3 and negative strains ($s_e^i = -1$: contraction) around these channels, leading to a significant widening of the channels to the outlet ports 2 and 3. The area of the domain that coincides with the channel to outlet 1 shows negative strains, i.e. the channel to outlet 1 contracts.

The optimized support layout is depicted in Fig. 25. It shows that mainly the boundaries on the right and top edges are fixed, while the main bulk of the design space is unsupported. The small areas of high support stiffness within the interior of the domain are beneficial for the development of local areas of contraction/expansion, as depicted in Fig. 26. The elements with high support stiffness in between the two ellipses help to separate the area of contraction and expansion by bracing the structure.

8 Conclusions

An approach to topology optimization of FSI problems has been presented and applied to the multi-objective design optimization of dynamically tunable, elastically deforming micro fluidic devices. The proposed design method allows for optimizing the topology of the fluid channels in multi-layered structures, the thickness distribution of the structural layers, the layout of the active material, and the location of supports.

It was shown that for the class of problems considered in this paper, the structural deformations due to fluid forces are negligible in comparison to the deformations due to external and internal actuation. This allows considering only a one-sided structure-fluid coupling. As topology optimization gives only limited control over the resulting geometric features, the validity of this simplification should be verified for the resulting optimized design.

In order to alter the flow noticeably, large deformations are needed. Therefore, the structural response was modeled by a geometrically non-linear finite element model. To avoid issues due to large compressive loading, such as buckling, predominantly tensile loads have been considered in this study. However, compressive external and internal loads are expected to be particularly efficient in altering channel flows and remain to be studied in the future. The current study employs a linear stress-strain relation. To account for large strains a non-linear constitutive model such as a hyper-elastic model should be used. Due to the separate treatment of fluid and structural domain this could be easily incorporated in the existing framework.

In this study, a simple 2-D flow model has been considered. To capture the influence of bottom and top structural layers on the flow, refined fluid models need to be applied. Again this could be implemented without changing the overall computational framework. The fluid-solid interfaces are described via a porosity approach, which approximates the flow characteristics sufficiently well for low Reynolds number flows. However, for high Reynolds numbers, the stair-step interface geometry will likely cause problems.

The proposed method describes the structural deformations on a Lagrangian mesh and the flow is predicted on a

fixed Eulerian mesh. While in this paper a hydrodynamic lattice Boltzmann method was used, any finite element or finite volume flow solvers can be integrated into the proposed computational framework. The separation of structure and flow solver allows the use of standard analysis tools. In particular, it circumvents the need for fluid analysis methods capable of operating on moving meshes. However, a mapping method is needed to transform the structural density distribution into a impermeability distribution defining the layout in the undeformed and deformed configurations. In numerical studies the proposed simple geometric mapping approach was shown to be robust and computationally inexpensive.

Three numerical studies on the design of tunable manifolds have demonstrated that the proposed method is well suited for topology optimization of fluid-structure systems. While most micro-fluidic applications are dominated by low Reynolds number flows allowing for a one-sided FSI model, two-way coupling needs to be considered in general.

Acknowledgments The authors acknowledge the support of the National Science Foundation under grant DMI-0348759. The opinions and conclusions presented in this chapter are those of the authors and do not necessarily reflect the views of the sponsoring organization.

References

- Aage N, Poulsen TH, Gersborg-Hansen A, Sigmund O (2008) Topology optimization of large scale Stokes flow problems. *Struct Multidiscipl Optim* 35(2):175–180. doi:10.1007/s00158-007-0128-0
- Andreasen SC, Gersborg AR, Sigmund O (2009) Topology optimization of microfluidic mixers. *Int J Numer Methods Fluids* 61(5):498–513. doi:10.1002/fld.1964
- Babuška I (1973) The finite element method with penalty (variational principle with penalty for finite element solution of model Poisson equation with homogeneous Dirichlet boundary conditions, noting convergence). *Math Comput* 27:221–228
- Bar-Cohen Y (2004) Electroactive polymer (EAP) actuators as artificial muscles—reality, potential, and challenges. Bellingham SPIE—The International Society for Optical Engineering
- Belytschko T, Liu WK, Moran B (2005) *Nonlinear finite elements for continua and structures*. Wiley, New York
- Bendsøe MP, Sigmund O (2003) *Topology optimization: theory, methods and applications*. Springer, Heidelberg
- Borrvall T, Petersson J (2003) Topology optimization of fluids in Stokes flow. *Int J Numer Methods Fluids* 41(1):77–107. doi:10.1002/fld.426
- Buhl T (2002) Simultaneous topology optimization of structure and supports. *Struct Multidiscipl Optim* 23(5):336–346. doi:10.1007/s00158-002-0194-2
- Chen S, Doolen GD (1998) Lattice Boltzmann method for fluid flows. *Annu Rev Fluid Mech* 30:329–364
- Dimitrov D, Schreve K, de Beer N (2006) Advances in three dimensional printing—state of the art and future perspectives. *Rapid Prototyping J* 12(3):136–147
- Evgrafov A (2006) Topology optimization of slightly compressible fluids. *ZAMM* 86(1):46–62. doi:10.1002/zamm.200410223
- Evgrafov A, Pingen G, Maute K (2008) Topology optimization of fluid domains: kinetic theory approach. *ZAMM* 88(2):129–141. doi:10.1002/zamm.200700122
- Gersborg-Hansen A, Sigmund O, Haber RB (2005) Topology optimization of channel flow problems. *Struct Multidiscipl Optim* 30(3):181–192. doi:10.1007/s00158-004-0508-7
- Guest JK, Prévost JH (2006) Optimizing multifunctional materials: design of microstructures for maximized stiffness and fluid permeability. *Int J Solids Struct* 43(22–23):7028–7047. doi:10.1016/j.ijsolstr.2006.03.001
- Kim H, Lee HBR, Maeng WJ (2009) Applications of atomic layer deposition to nanofabrication and emerging nanodevices. *Thin Solid Films* 517(8):2563–2580
- Klimetzek FR, Paterson J, Moos O (2006) Autoduct: topology optimization for fluid flow. In: *Proceedings of Konferenz für angewandte Optimierung*. Karlsruhe, Germany
- Maute K, Allen M (2004) Conceptual design of aeroelastic structures by topology optimization. *Struct Multidiscipl Optim* 27:27–42
- Maute K, Reich GW (2006) Integrated multidisciplinary topology optimization approach to adaptive wing design. *AIAA J Aircr* 43(1):253–263
- Moos O, Klimetzek FR, Rossmann R (2004) Bionic optimization of air-guiding systems. In: *Proceedings of SAE 2004 world congress & exhibition*. Detroit, MI
- Niklaus F, Stemme G, Lu J-Q, Gutmann RJ (2006) Adhesive wafer bonding. *J Appl Phys* 99(3):031101
- Othmer C (2008) A continuous adjoint formulation for the computation of topological and surface sensitivities of ducted flows. *Int J Numer Methods Fluids* 58(8):861–877. doi:10.1002/fld.1770
- Othmer C, Klimetzek T, Giering R (2006) Computation of topological sensitivities in fluid dynamics: cost function versatility. In: *Proceedings of ECCOMAS CFD*. Delft, Netherlands
- Pingen G (2008) *Optimal design for fluidic systems: topology and shape optimization with the lattice Boltzmann method*. PhD thesis, University Of Colorado at Boulder
- Pingen G, Evgrafov A, Maute K (2006) Towards the topology optimization of fluid-structure interaction problems with immersed boundary techniques. In: *NSF design, service, and manufacturing grantees and research conference*, St. Louis, Missouri
- Pingen G, Evgrafov A, Maute K (2007a) Topology optimization of flow domains using the lattice Boltzmann method. *Struct Multidiscipl Optim* 36(6):507–524. doi:10.1007/s00158-007-0105-7
- Pingen G, Waidmann M, Evgrafov A, Maute K (2007b) Application of a parametric level-set approach to topology optimization fluid with the Navier–Stokes and lattice Boltzmann equations. In: *Proceedings of the 7th world congress of structural and multidisciplinary optimization*, 21–25 May 2007, Seoul, Korea, ISSMO
- Pingen G, Evgrafov A, Maute K (2009a) Adjoint parameter sensitivity analysis for the hydrodynamic lattice Boltzmann method with applications to design optimization. *Comput Fluids* 38(4):910–923. doi:10.1016/j.compfluid.2008.10.002
- Pingen G, Waidmann M, Evgrafov A, Maute K (2009b) A parametric level-set approach for topology optimization of flow domains. *Struct Multidiscipl Optim*. doi:10.1007/s00158-009-0405-1
- Ramm E, Maute K, Schwarz S (1998a) Adaptive topology and shape optimization. In: *Proceedings of 4th world congress on computational mechanics*, 29 June–2 July. Mendoza, Argentina, pp 19–38
- Ramm E, Maute K, Schwarz S (1998b) Conceptual design by structural optimization. In: *Proceedings of EURO-C*, 31 March–3 April. Badgastein, Austria, pp 879–896
- Spaid MAA, Phelan FR (1997) Lattice Boltzmann methods for modeling microscale flow in fibrous porous media. *Phys Fluids* 9(9):2468–2474
- Stadler W (1988) *Multicriteria optimization in engineering and in the sciences*. Springer, Heidelberg

- Succi S (2001) *The lattice Boltzmann equation: for fluid dynamics and beyond*. Oxford University Press, Oxford
- Svanberg K (1995) A globally convergent version of MMA without linesearch. In: *Proceedings of the first world congress of structural and multidisciplinary optimization*, 28 May–2 June 1995, pp 9–16, Goslar, Germany
- Yoon GH (2009) Topology optimization for stationary fluid-structure interaction problems using a new monolithic formulation. In: *Proceedings of 8th world congress on structural and multidisciplinary optimization*, Lisbon, Portugal
- Yu D, Mei R, Luo LS, Shyy W (2003) Viscous flow computations with the method of lattice Boltzmann equation. *Prog Aerosp Sci* 39(5):329–367. doi:[10.1016/S0376-0421\(03\)00003-4](https://doi.org/10.1016/S0376-0421(03)00003-4)
- Zhang XQ, Lowe C, Wissler M, Jahne B, Kovacs G (2005) Dielectric elastomers in actuator technology. *Adv Eng Mater* 7(5): 361–367